

The density of dark matter haloes of early-type galaxies in low-density environments

E. M. Corsini^{1,2*}, G. A. Wegner^{3†}, J. Thomas⁴, R. P. Saglia⁴ and R. Bender^{4,5}

¹*Dipartimento di Fisica e Astronomia ‘G. Galilei’, Università di Padova, vicolo dell’Osservatorio 3, 35122 Padova, Italy*

²*INAF–Osservatorio Astronomico di Padova, vicolo dell’Osservatorio 2, 35122 Padova, Italy*

³*Department of Physics and Astronomy, 6127 Wilder Laboratory, Dartmouth College, Hanover, NH 03755-3528, USA*

⁴*Max-Planck-Institut für extraterrestrische Physik, Giessenbachstraße, D-85748 Garching, Germany*

⁵*Universitäts-Sternwarte München, Scheinerstraße 1, D-81679 München, Germany*

Accepted 2016 November 9. Received 2016 November 9; in original form 2016 July 20

ABSTRACT

New photometric and long-slit spectroscopic observations are presented for NGC 7113, PGC 1852, and PGC 67207 which are three bright galaxies residing in low-density environments. The surface-brightness distribution is analysed from the K_S -band images taken with adaptive optics at the Gemini North Telescope and the $ugriz$ -band images from the Sloan Digital Sky Survey while the line-of-sight stellar velocity distribution and line-strength Lick indices inside the effective radius are measured along several position angles. The age, metallicity, and α -element abundance of the galaxies are estimated from single stellar-population models. In spite of the available morphological classification, images show that PGC 1852 is a barred spiral which we do not further consider for mass modelling. The structural parameters of the two early-type galaxies NGC 7113 and PGC 67207 are obtained from a two-dimensional photometric decomposition and the mass-to-light ratio of all the (luminous and dark) mass that follows the light is derived from orbit-based axisymmetric dynamical modelling together with the mass density of the dark matter halo. The dynamically derived mass that follows the light is about a factor of 2 larger than the stellar mass derived using stellar-population models with Kroupa initial mass function. Both galaxies have a lower content of halo dark matter with respect to early-type galaxies in high-density environments and in agreement with the predictions of semi-analytical models of galaxy formation.

Key words: galaxies: abundances — galaxies: elliptical and lenticular, cD — galaxies: formation — galaxies: haloes — galaxies: kinematics and dynamics — galaxies: stellar content

1 INTRODUCTION

A comprehensive picture of galaxy formation and evolution requires understanding the assembly and growth of massive early-type galaxies (ETGs). These systems dominate the bright end of the luminosity function (Bernardi et al. 2010), contain most of the present-day stellar mass (Fukugita et al. 1998), and can be observed out to high redshifts (Daddi et al. 2005). The central dark matter (DM) density, stellar mass-to-light ratio, and distribution of stellar orbits provide valuable clues on the epoch and mechanism of the assembly of ETGs.

Both theoretical arguments and numerical simulations predict a relationship between the concentration and assembly epoch of the DM haloes with denser haloes formed earlier (Wechsler et al. 2002). The halo mass distribution also depends on the interplay between baryons and DM. Indeed the central DM and stellar mass profile could become similar as the result of violent relaxation (Hilz et al. 2012), whereas adiabatic contraction is able to increase the amount of DM in the galaxy centres lowering the amount of the stellar mass (Gnedin et al. 2004). The stellar mass-to-light ratio is set by the initial mass function (IMF) which determines the mass scale and chemical enrichment of galaxies too. The systematic variation of the IMF with the galaxy mass in ETGs results from the analysis of integrated spectra (van Dokkum & Conroy 2010; Spiniello et al. 2012; Ferreras et al. 2013; La Barbera et al. 2013; Smith et al. 2015), stellar dynamics (Thomas et al. 2011;

* E-mail: enricomaria.corsini@unipd.it

† Visiting Astronomer, MDM Observatory, Kitt Peak, Arizona, operated by a consortium of Dartmouth College, University of Michigan, Columbia University, The Ohio State University, and Ohio University.

Cappellari et al. 2012; Wegner et al. 2012; Barnabè et al. 2013; Tortora et al. 2013), scaling relations (Dutton et al. 2013), and gravitational lensing (Auger et al. 2010; Treu et al. 2010) and it is interpreted with an enhanced fraction of low-mass stars in more massive galaxies. Recently, Martín-Navarro et al. (2015) have found that the IMF in massive ETGs strongly depends on galactocentric distance with the excess of low-mass stars confined into the central regions and implying a difference between the formation process of the core and outer regions.

Numerical simulations and semi-analytical models predict, on the other hand, that environment also plays an important role in setting the properties of galaxies (e.g., Kauffmann et al. 2004). DM haloes in low-density environments assemble and virialize later with respect to their equal mass counterparts in high-density environments (e.g., Hahn et al. 2007). As a consequence, galaxies in low-density regions could have younger stellar populations than their mass analogous in clusters of galaxies (e.g., Bernardi et al. 1998; De Lucia & Blaizot 2007). In general, the population of galaxies in voids is dominated by small and faint late-type spirals which are gas rich and star forming. But, some massive ETGs with stellar mass $M_* > 10^{10} M_\odot$ and no active star formation in the last several Gyrs are also present (Croton et al. 2005; Beygu et al. 2017). They have similar properties on average of galaxies living in field or clusters and hosted by DM haloes of similar mass suggesting comparable mass assembly and quenching process (Croton & Farrar 2008; Penny et al. 2015). In particular, the lack of difference in the star formation rates of massive galaxies independently of their environment points to quenching being a mass-related effect (Fraser-McKelvie et al. 2016). Studying in detail the mass distribution and properties of stellar populations of galaxies in voids provides a direct insight on their assembly and quenching histories. However, except for a few objects (e.g., Rieder et al. 2013), not much is known about the density of DM haloes of galaxies in voids and low-density environments. In particular, orbit-based dynamical models aimed at constraining the dark and luminous mass distribution within the half-light radius r_{eff} of large samples of ETGs from long-slit or integral-field stellar kinematics considered only galaxies in field, groups, and clusters (Cappellari et al. 2006; Thomas et al. 2007, 2014, Zhu et al., in preparation). Here, we present our first attempt to tackle this issue.

This study complements our earlier works on ETGs in Coma and Abell 262 clusters (Thomas et al. 2007, 2011; Wegner et al. 2012), which we selected to be respectively a rich and a poor nearby cluster at about the same distance. As a consequence, the spatial resolution of the photometric and kinematic data, which consist of broad-band images and long-slit spectra obtained along various position angles, is comparable for all the sample galaxies (Mehlert et al. 2000; Wegner et al. 2002, 2012; Corsini et al. 2008). We derived the dynamical mass-to-light ratio of the mass that follows light and DM halo parameters from axisymmetric orbit-based dynamical models in combination with the stellar mass-to-light ratio, age, metallicity, and α -elements abundance from single stellar population models. The DM fraction of total mass inside r_{eff} is significant ($f_{\text{DM,dyn}} \approx 0.2 - 0.5$) in most of the sample ETGs. Their haloes are about 10 times denser than in spirals of the same stellar mass

and assembled at larger redshifts ($z_{\text{DM}} \approx 1 - 3$) and match with constraints from stellar populations. The stars of some galaxies appear to be younger than the halo, which indicates a secondary star-formation episode after the main halo assembly. The dynamical mass that follows the light is larger than expected for a Kroupa IMF, especially in galaxies with high velocity dispersion σ_{eff} inside r_{eff} . Some of them show a negligible DM fraction. This could indicate a Salpeter IMF in massive ETGs. Alternatively, some of the DM in massive galaxies could follow the light very closely suggesting a significant degeneracy between dark and luminous matter or the assumption of a constant stellar mass-to-light ratio inside a galaxy should be relaxed. These findings can be easily compared to those for ETGs in low-density environments since the data sets are similar and we analysed them with the same dynamical and stellar population models.

The structure of the paper is as follows. In Section 2, we discuss the selection of the sample galaxies. In Section 3, we describe the imaging data set and perform the isophotal analysis and photometric decomposition. In Section 4, we present the spectroscopic data set and measure the stellar kinematics and line-strength indices along different axes and derive the properties of the stellar populations. In Section 5, we discuss the results of the dynamical modelling. In Section 6, we draw our conclusions.

2 SAMPLE SELECTION

As a pilot project, we have endeavoured to study in more detail three objects randomly chosen from the list of Wegner & Grogin (2008) who focused on 26 ETGs within and bordering three prominent nearby voids at $cz \approx 5000 - 10000 \text{ km s}^{-1}$ in the Second Center for Astrophysics Redshift Survey (CfA2; Geller & Huchra 1989). The galaxies were selected to be ellipticals or lenticulars based on their morphology in the blue images of the Second Palomar Observatory Sky Survey (POSS-II) and to be located in underdense regions, where the smoothed galaxy number density is lower than the mean density for the CfA2 survey as defined in Grogin & Geller (1999). Wegner & Grogin (2008) found that while the oldest ETGs in voids and Coma cluster have comparable ages, the age range of void ETGs is wider and several objects are younger and show undergoing star formation.

Table 1 lists the properties of the selected galaxies. We quote the B - and R -band total magnitudes that are about a magnitude brighter than the values given in Wegner & Grogin (2008); this stems mainly from our choice of distances, that are based on systemic velocities with respect to the cosmic microwave background reference frame and the concordance cosmology ($H_0 = 73 \text{ km s}^{-1} \text{ Mpc}^{-1}$, $\Omega_m = 0.27$, $\Omega_\Lambda = 0.73$). We also give the smoothed density contrast derived by Grogin & Geller (1999), who included PGC 1852 into their lowest density ($n/\bar{n} < 0.5$) and NGC 7113 and PGC 67207 into their higher density ($0.5 < n/\bar{n} < 1$) void subsamples. Different void algorithms qualitatively give similar results but differ a lot in the details of the edge locations (Colberg et al. 2008). According to Kreckel et al. (2011), only a few of the galaxies from Grogin & Geller (1999) are located in extremely underdense void interiors. Kreckel et al. (2011) could derive

the filtered density contrast only for the galaxies falling in sky regions with an extended uniform coverage of the Sloan Digital Sky Survey (SDSS) Data Release 7 (DR7; Abazajian et al. 2009). This is not the case for our objects and we decided to estimate their filtered density contrast ($-0.4 < \delta < 1.6$) from an outlier-resistant linear regression correlating the density contrast of Grogin & Geller (1999) to that of Kreckel et al. (2011). We conclude that our sample galaxies are more probably reside in the low-density outskirts of voids rather than being located in their desolately underdense central regions.

PGC 1852 was initially included based on earlier POSS morphological classification as an elliptical galaxy, but improved imaging reveals that it is a barred spiral and it has been excluded from the dynamical analysis, although we include the photometric and spectroscopic data here.

3 BROAD-BAND IMAGING

3.1 Sloan Digital Sky Survey imaging

We retrieved the *ugriz*-band images of the sample galaxies from the Data Archive Server (DAS) of the SDSS DR9 (Ahn et al. 2012).

All the archive images were already bias subtracted, flat-field corrected, sky subtracted, and flux calibrated according to the associated calibration information stored in the DAS. We trimmed the images selecting a field of view (FOV) of 400×400 pixel (corresponding to 2.6×2.6 arcmin²) centred on the galaxies.

To estimate the goodness of the SDSS sky subtraction, we fitted elliptical isophotes with the algorithm by Bender & Moellenhoff (1987) to measure the radial profile of the azimuthally-averaged surface brightness of the galaxies at large radii. We masked foreground stars, nearby and background galaxies, residual cosmic rays, and bad pixels before fitting the isophotes. As a first step, we allowed to vary the centres, ellipticities, and position angles of ellipses. Then, we adopted the centre of the inner ellipses ($a < 5$ arcsec) and the ellipticity and position angle of the outer ones ($a > 10$ arcsec). We assumed the constant value of the surface brightness at large radii ($a \sim 70$ arcsec) as the residual sky level to be subtracted from the image. We measured the standard deviation of the image background after sky subtraction, σ_{sky} , in regions free of sources at the edges of the FOV.

3.2 Gemini North Telescope imaging

To map the central surface brightness distribution with a higher spatial resolution with respect to that of the SDSS images, NGC 7113 and PGC 67207 were observed with the Near Infrared Imager (NIRI; Hodapp et al. 2003) in combination with the Altitude Conjugate Adaptive Optics for the Infrared (ALTAIR; Christou et al. 2010) and laser guide star (LGS; Boccas et al. 2006) system on the 8.2 m Gemini North Telescope on 2011 August 16 and October 16, respectively.

The $f/32$ focus was employed with a 1024×1024 pixel ALLADIN-II InSb array as the detector, which gave a 22.5×22.5 arcsec² FOV with a plate scale of 0.022 arcsec

pixel⁻¹. A K_s filter ranging from 1.99 and 2.30 μm and centred on 2.15 μm was used for all the observations, the field lens of the instrument was placed ‘in’, and the Cassegrain rotator was set to ‘following’. NGC 7113 and a PSF standard star at a distance of 1.9 arcmin were observed with 10 s exposures. A total of 62, 25, and 14 useable exposures were collected for the galaxy, sky, and PSF standard star, respectively. PGC 67207 and a PSF standard star at a distance of 2.7 arcmin were observed with 15 s and 10 s exposures, respectively. A total of 14, 12, and 12 exposures were secured for the galaxy, sky, and PSF standard star, respectively. A five-pointing dither pattern with 2.0 arcsec offsets was used for each set of observations. The sky frames were obtained at a distance of about 2.0 arcmin from the target galaxy. The flux standard star FS 152 was also observed, but its images were not analysed because the flux calibration was performed by fitting the surface-brightness radial profiles measured in the Gemini images to the SDSS ones. Flat-field and dark frames were provided on the same day as the target observations using the same readout mode and exposure times.

We reduced the images using the NIRI tasks of the Gemini IRAF¹ reduction package. Briefly, these included NPREDPARE which set up the image headers, NIFLAT and NISKY which created flat-field and sky frames from the individual observations, respectively, NIREDUCE which subtracted the sky frame from the galaxy images and divided them by the flat-field frame, and IMCOADD which aligned and co-added the dithered galaxy images and removed distortion effects.

Fig. 1 shows the final high-resolution images for NGC 7113 and PGC 67207.

3.3 Isophotal analysis

We fitted the isophotes of the sample galaxies in the SDSS and *Gemini* images using the algorithm by Bender & Moellenhoff (1987). We allowed the centres of the ellipses free to vary and considered the deviation of the isophotal shape from a perfect ellipse to obtain the radial profiles of the azimuthally-averaged surface brightness, μ , ellipticity, ϵ , position angle, P.A., centre coordinates, x_0 and y_0 , and third, fourth, and sixth cosine Fourier coefficients, a_3 , a_4 , and a_6 , and third, fourth, and sixth sine Fourier coefficients, b_3 , b_4 , and b_6 .

We derived the $u - g$, $g - r$, $r - i$, and $i - z$ surface-brightness radial profiles from the SDSS images and we measured the radial profiles of all the isophotal parameters in the r band for all the sample galaxies. We found that the Gemini images are affected by a PSF that strongly varies with the distance from the FOV centre. Indeed, we performed a two-dimensional Moffat fit (Moffat 1969) to the PSF standard stars and to the two faint stars visible in the FOV of NGC 7113 and PGC 67207 at a distance of about 5 arcsec from the galaxy centre. While the on-axis images of the PSF standard stars were round (FWHM = 0.11 arcsec,

¹ The Imaging Reduction and Analysis Facility (IRAF) is distributed by the National Optical Astronomy Observatory, which is operated by the Association of Universities for Research in Astronomy (AURA), Inc., under cooperative agreement with the National Science Foundation.

Table 1. Properties of the sample galaxies.

Object	Alt. name	Type	V_{CMB} (km s ⁻¹)	D_A (Mpc)	$(m - M)_L$ (mag)	M_B (mag)	M_R (mag)	n/\bar{n}
(1)	(2)	(3)	(4)	(5)	(6)	(7)	(8)	(9)
NGC 7113	CGCG 2140.0 + 1221	S0	5405	72.5	34.38	-20.07	-21.60	0.68
PGC 1852	CGCG 0027.9 + 0536	E2	6737	89.9	34.86	-19.78	-21.18	0.37
PGC 67207	CGCG 2140.0 + 1340	E2	5044	67.7	34.23	-19.52	-20.97	0.82

Note. Column (1): galaxy name. Column (2): alternative name. Column (3): morphological type from Wegner & Grogin (2008). In spite of the E2 classification, PGC 1852 is a barred spiral galaxy. Column (4): systemic velocity with respect to the cosmic microwave background (CMB) reference frame from the NASA/IPAC Extragalactic Database (NED). Column (5): angular distance from NED adopting $H_0 = 73 \text{ km s}^{-1} \text{ Mpc}^{-1}$, $\Omega_m = 0.27$, and $\Omega_\Lambda = 0.73$. Column (6): distance modulus from the luminosity distance in NED. Column (7): absolute magnitude in the Johnson-Cousins B band from the apparent magnitude within the $\mu_B = 26 \text{ mag arcsec}^{-2}$ isophote measured by Grogin & Geller (1999) and after applying the Galactic absorption correction (Schlafly & Finkbeiner 2011) and K_B correction (Chilingarian et al. 2010) available in NED. Column (8): absolute magnitude in the Johnson-Cousins R band from the apparent magnitude within the $\mu_R = 26 \text{ mag arcsec}^{-2}$ isophote measured by Grogin & Geller (1999) and after applying the Galactic absorption correction (Schlafly & Finkbeiner 2011) and K_R correction (Chilingarian et al. 2010) available in NED. Column (9): smoothed density contrast calculated with an uncertainty $\lesssim 0.1$ by Grogin & Geller (1999).

$\beta = 2.4$), the off-axis stellar images were highly elongated ($1 - b/a = 0.1$ for the star in the FOV of NGC 7113, 0.2 for the star in the FOV of PGC 67207) and tilted. Therefore, we derived only the surface-brightness radial profile from the *Gemini* images of NGC 7113 and PGC 67207.

We matched the surface-brightness radial profiles measured in the *Gemini* images to the SDSS ones by determining the zero-point and sky value of the high-resolution images that minimize the surface-brightness flux differences with the low-resolution images. The resulting distribution of the differences $\Delta m = r - K_s$ after minimization gives a mean $\langle \Delta m \rangle = -0.001 \text{ mag}$ and a standard deviation $\sigma_{\Delta m} = 0.012 \text{ mag}$ for NGC 7113 between 2 and 7 arcsec and $\langle \Delta m \rangle = 0.003 \text{ mag}$ and $\sigma_{\Delta m} = 0.017 \text{ mag}$ for PGC 67207 between 1 and 4 arcsec. We concluded that NGC 7113 and PGC 67207 have no $r - K_s$ colour gradient in the matched radial region and the scatter $\sigma_{\Delta m}$ is the dominant source of error in the zero-point of the Gemini images because the SDSS DR9 r images have a relative calibration error better than 0.01 mag (Padmanabhan et al. 2008).

The r -band radial profiles of the azimuthally averaged surface brightness, ellipticity, position angle, centre coordinates and third, fourth, and sixth cosine and sine Fourier coefficients of the sample galaxies are presented in Fig. 2. They are the combination of the Gemini and SDSS data in the r band for NGC 7113 and PGC 67207. The r -band SDSS isophotal radial profiles of the sample galaxies are reported in Table A1. The Gemini surface-brightness radial profiles obtained in the r band for NGC 7113 and PGC 67207 are given in Table A2. The reported surface brightnesses are not corrected for cosmological dimming, Galactic absorption, and K correction.

3.4 Photometric decomposition

We derived the structural parameters of NGC 7113 and PGC 67207 by applying the Galaxy Surface Photometry Two-Dimensional Decomposition (GASP2D) algorithm (Méndez-Abreu et al. 2008, 2014) to the SDSS r -band images.

We modelled the surface brightness of both galaxies using a Sérsic function (Sérsic 1968)

$$I(x, y) = I_e e^{-b_n [(r/r_e)^{1/n} - 1]}, \quad (1)$$

where (x, y) are coordinates of each image pixel, r_e is the effective radius, I_e is the surface brightness at r_e , n is a shape parameter that describes the curvature of the radial profile, and $b_n = 1.9992n - 0.3271$ for $0.5 < n < 10$ (Ciotti 1991). The galaxy model was assumed to have elliptical isophotes centred on (x_0, y_0) with constant position angle PA and constant axial ratio q . Therefore, the distance r of each image pixel from the galaxy centre is

$$r(x, y) = \left[(-\Delta x \sin \text{PA} + \Delta y \cos \text{PA})^2 - (\Delta x \cos \text{PA} - \Delta y \sin \text{PA})^2 / q^2 \right]^{1/2}, \quad (2)$$

where $\Delta x = x - x_0$ and $\Delta y = y - y_0$. The total luminosity of the model galaxy is

$$L_T = 2\pi n (1 - q) I_e r_e^2 e^{b_n} b_n^{-2n} \Gamma(2n) \quad (3)$$

where Γ is the complete gamma function.

To obtain the best-fitting structural parameters I_e , r_e , n , PA, and q and the position of the galaxy centre (x_0, y_0) , we took into account the seeing effects by convolving the model image with a circular Moffat PSF with the shape parameters measured directly from stars in the galaxy images. We found FWHM = 0.96 arcsec and $\beta = 4.0$ for NGC 7113 and FWHM = 0.99 arcsec and $\beta = 2.7$ for PGC 67207. We fitted both images out to a surface brightness level of $1.5\sigma_{\text{sky}}$ corresponding to $\mu_r = 24.1 \text{ mag arcsec}^{-2}$. We adopted the same masks built for fitting the isophotes and excluded the masked pixels from the fit.

We estimated the errors on the best-fitting parameters by generating a set of 200 images of galaxies with a Sérsic surface-brightness radial profile and total apparent magnitude $12 \leq m_r \leq 14 \text{ mag}$. We randomly chose the structural parameters of the artificial galaxies to cover the ranges obtained for our galaxies. We adopted the values of the pixel scale ($0.396 \text{ arcsec pixel}^{-1}$), gain ($4.8 e^- \text{ ADU}^{-1}$), readout noise ($5.6 e^- \text{ rms}$), and exposure time (53.9 s) to mimic the instrumental setup of the photometric observations. We

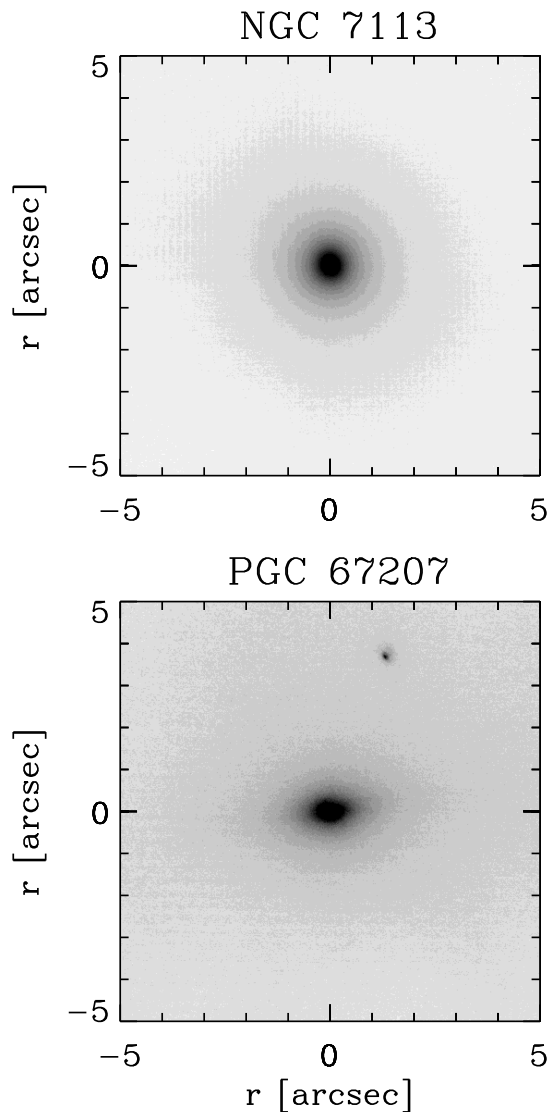


Figure 1. Central portions of the Gemini images of NGC 7113 (top panel, 1 arcsec = 351.5 pc) and PGC 67207 (bottom panel, 1 arcsec = 328.2 pc). Each frame uses a negative intensity scale and north is at the top with east to the left.

added to the artificial images a background level (120 ADU) and photon noise to yield a signal-to-noise ratio (S/N) similar to that of the observed ones. We adopted a Moffat PSF with $\text{FWHM} = 0.98$ arcsec and $\beta = 3.3$. Finally, we analysed the images of the artificial galaxies with GASP2D and calculated the relative errors on the fitted parameters. We derived the mean and standard deviation of the relative errors for the artificial galaxies of each magnitude bin and we adopted them as the systematic and statistical errors for the best-fitting parameters of the observed galaxies according to their apparent magnitude.

Fig. 3 shows the r -band SDSS image, GASP2D best-fitting image, and residual image of NGC 7113 and

PGC 67207, respectively. Their best-fitting structural parameters are collected in Table 2. The effective surface brightnesses are corrected for cosmological dimming, Galactic absorption, and K correction and the total magnitudes of the Sérsic models are given after applying the Galactic absorption and K corrections. For both galaxies, we found that the best-fitting Sérsic function is a good representation of the combined Gemini-SDSS surface-brightness radial profile (Fig. 2). Therefore, we adopted such a parametric representation for the dynamical modelling of the two galaxies.

4 LONG-SLIT SPECTROSCOPY

4.1 Observations and data reduction

Long-slit spectroscopic data of the sample galaxies were obtained with the 2.4-m Hiltner telescope of the MDM Observatory at Kitt Peak, Arizona, during four different runs between 2003 and 2012. Details of the instrumental set-up of the observations carried out on 2003 November 18-21 (run 1), 2005 November 01 (run 2), 2006 November 13-16 (run 3), and 2012 September 24-25 (run 4) are given in Table 3.

The sample galaxies were observed along different axes crossing the nucleus. At the beginning of each exposure the galaxy was centred on the slit using the guiding camera. NGC 7113 was observed in two different runs at position angle $\text{P.A.} = 0^\circ$ to perform a consistency check between the measurements of stellar kinematics and line-strength indices. The integration times of each exposure, total integration times, and slit position angle of the galaxy spectra are given in Table 4.

In each run, a number of G and K giant stars were selected from the samples by Faber et al. (1985) and González (1993) and observed to use their spectra as templates in measuring the line-strength indices. In addition, different spectra of at least one spectrophotometric standard star per night were obtained to calibrate the flux of the galaxy and template star spectra before line-strength indices were measured. A spectrum of the comparison arc lamp was taken before and/or after each object exposure to allow an accurate wavelength calibration. Bias exposures and quartz-lamp flat-field spectra were acquired in the afternoon before each observing night.

We performed the reduction of the spectroscopic data using standard IRAF routines. We bias subtracted, flat-field corrected, corrected for cosmic rays and bad columns, wavelength calibrated, corrected for CCD misalignment, sky subtracted, and flux calibrated all the spectra. No pixel binning was adopted. After bias subtraction, we corrected the spectra for pixel-to-pixel sensitivity variations by using an averaged and normalized flat-field for each night. We identified and corrected cosmic rays by interpolating over with the LACOS_SPEC task (van Dokkum 2001). We corrected the residual cosmic rays by manually editing the spectra. Bad columns were replaced by linearly interpolating over adjacent columns. We rebinned each spectrum using the wavelength solution obtained from the corresponding arc-lamp spectrum. We checked the accuracy of the wavelength rebinning by measuring the rms of the difference between the derived and predicted wavelengths for the arc-lamp emission lines in the wavelength-calibrated comparison spectra. For

NGC 7113 – r

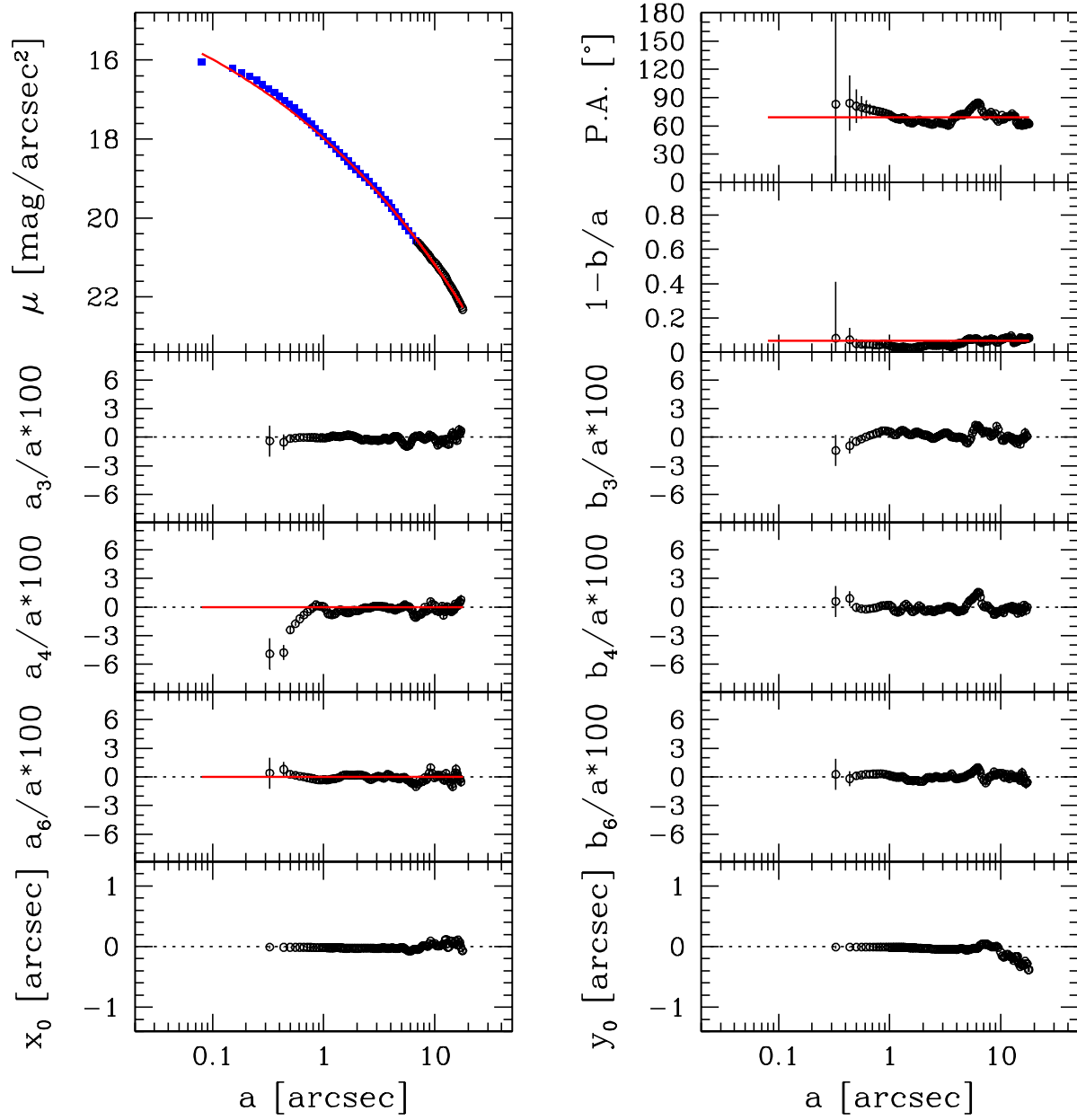
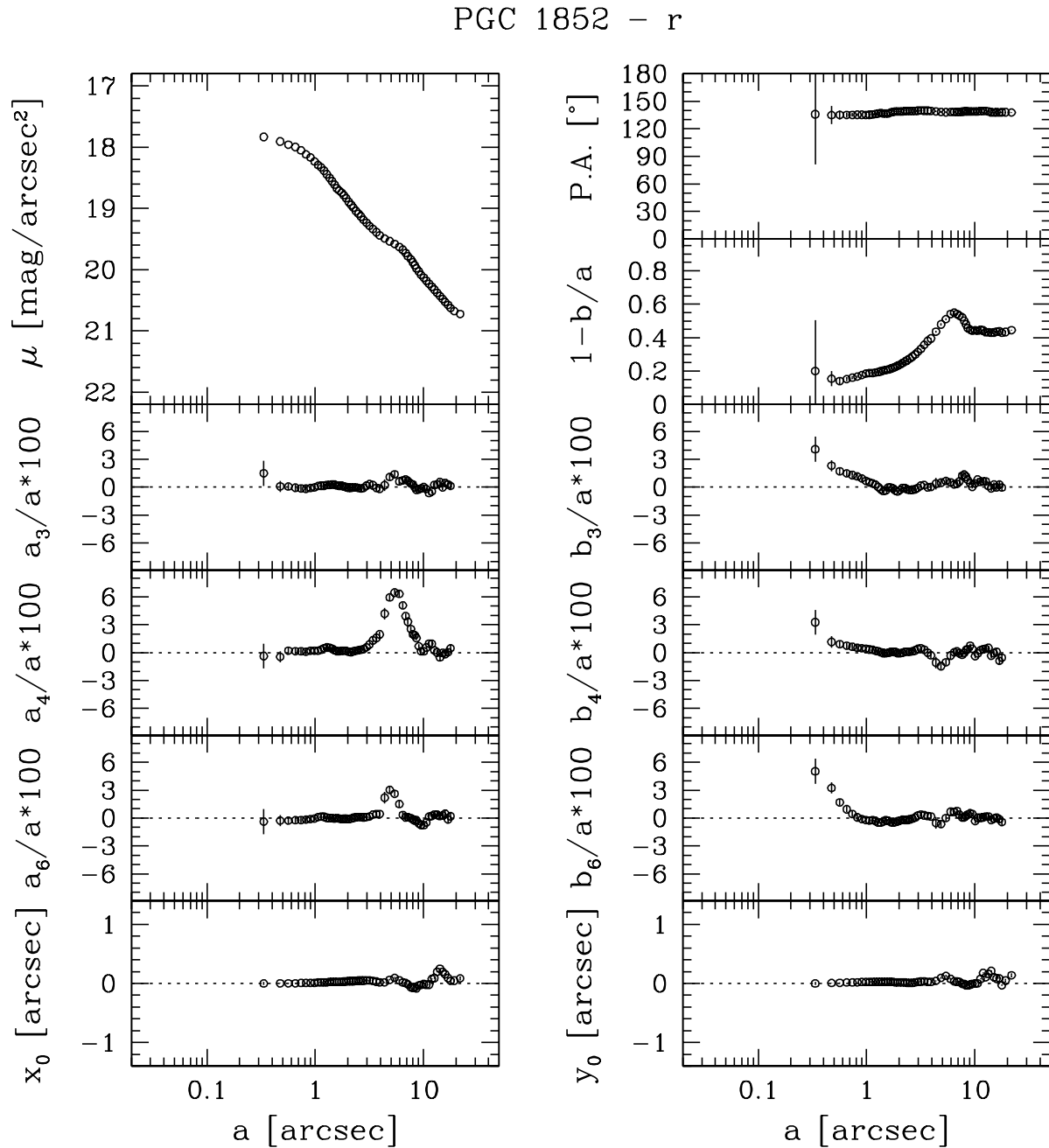


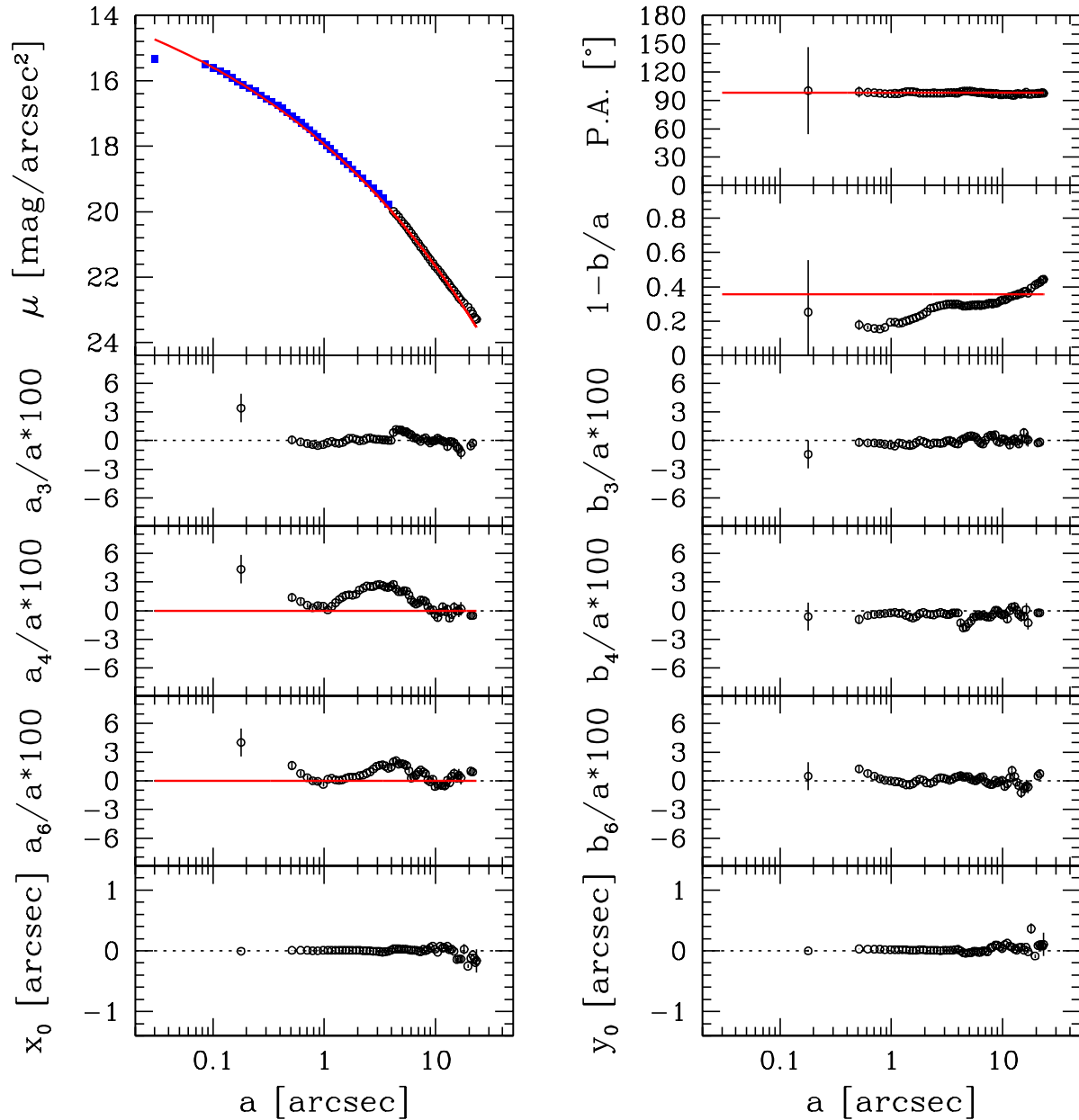
Figure 2. Isophotal parameters of the galaxies from *r*-band SDSS (black open circles) and Gemini images (blue filled squares) as a function of the logarithm of the semimajor-axis distance in arcsec. Left-hand panels (from top to bottom): radial profiles of surface brightness (μ), third- (a_3), fourth- (a_4), and sixth-order (a_6) cosine Fourier coefficients, and x -coordinate of the centre (x_0). Right-hand panels (from top to bottom): radial profiles of position angle (PA), ellipticity ($e = 1 - b/a$), third- (b_3), fourth- (b_4), and sixth-order (b_6) sine Fourier coefficients, and y -coordinate of the centre (y_0). For NGC 7113 and PGC 67207 the solid red lines correspond to the radial profiles of μ , PA, e , a_4 , and a_6 without the correction for seeing convolution which we obtained from the photometric decomposition and used in the dynamical modelling. The measured and model surface brightnesses are not corrected for cosmological dimming, Galactic absorption, and K correction.


 Figure 2. *continued*

all the runs the resulting rms is 0.05 \AA corresponding to 3 km s^{-1} at $H\beta$, while the systematic error of the wavelength calibration is smaller than 10 km s^{-1} . The latter was estimated from the wavelength of the night-sky emission lines which we identified in the galaxy spectra (Osterbrock et al. 1996). The instrumental resolution of each run is given in Table 3. It was derived as the mean of the Gaussian FWHMs measured for the unblended arc-lamp emission lines of the wavelength-calibrated comparison spectra. We corrected all the galaxy and star spectra for CCD misalignment and de-

termined the sky contribution by interpolating a one-degree polynomial along the outermost 20 arcsec at the two edges of the slit, where the galaxy or stellar light was negligible. The estimated sky level was subtracted from the spectra. We flux calibrated each galaxy and template star spectrum using the sensitivity function obtained from the spectra of the spectrophotometric standard star obtained in the corresponding night. Finally, we co-added the spectra obtained for the same galaxy along the same axis in each run by using the centre of the stellar continuum as reference. This allowed us to im-

PGC 67207 – r

Figure 2. *continued*

prove the S/N of the resulting two-dimensional spectrum. A one-dimensional spectrum was obtained for each template star and we deredshifted it to rest frame.

4.2 Stellar kinematics

We measured the line-of-sight velocity distribution (LOSVD) of the stellar component of the sample galaxies from the absorption lines in the observed wavelength ranges using the Penalized Pixel Fitting (PPXF;

Cappellari & Emsellem 2004) and Gas and Absorption Line Fitting (GANDALF; Sarzi et al. 2006) algorithms which we adapted to deal with MDM spectra. The LOSVD was assumed to be a Gaussian plus third- and fourth-order Gauss-Hermite polynomials (Gerhard 1993; van der Marel & Franx 1993).

We rebinned each galaxy spectrum along the dispersion direction to a logarithmic scale, and along the spatial direction to obtain an $S/N \geq 20$ per resolution element. For each radial bin, we built an optimal template spectrum by con-

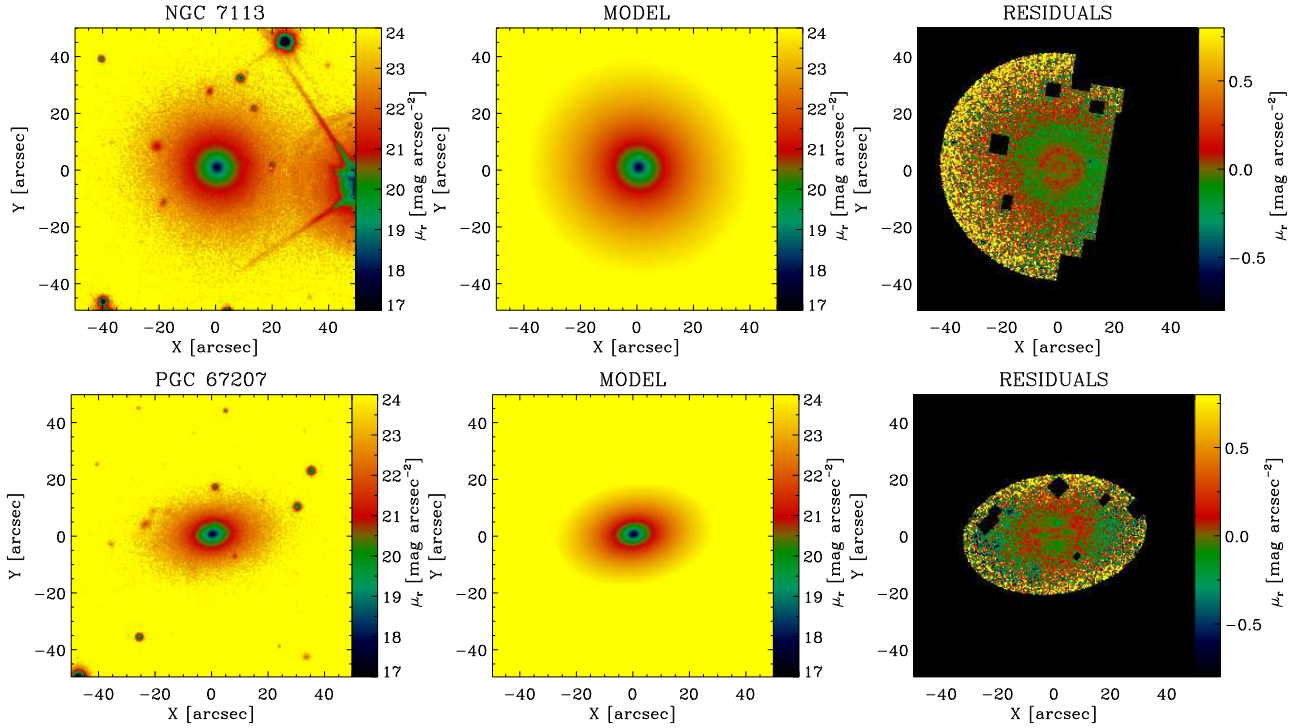


Figure 3. Two-dimensional photometric decomposition of NGC 7113 (top panels) and PGC 67207 (bottom panels). The SDSS r -band image (left-hand panel), best-fitting image (middle panel), and residual (i.e., observed-model) image (right-hand panel) are shown. The black areas in the residual images correspond to pixels excluded from the fitting procedure.

Table 2. The structural parameters of NGC 7113 and PGC 67207 from the photometric decomposition.

Object	$\mu_{\text{eff},r}$ (mag arcsec $^{-2}$)	r_{eff} (arcsec)	n	q	PA ($^{\circ}$)	m_r (mag)	M_r (mag)
(1)	(2)	(3)	(4)	(5)	(6)	(7)	(8)
NGC 7113	22.54 ± 0.02	24.83 ± 12.50	4.89 ± 0.47	0.932 ± 0.003	69.1 ± 0.1	12.23	-22.15
PGC 67207	21.71 ± 0.02	12.44 ± 6.26	5.18 ± 0.50	0.642 ± 0.003	97.8 ± 0.2	13.27	-20.96

Note. Column (1): galaxy name. Column (2): the SDSS r -band effective surface brightness corrected for cosmological dimming and after applying the Galactic absorption (Schlafly & Finkbeiner 2011) and K_r corrections (Chilingarian et al. 2010) available in NED. Column (3): effective radius. Column (4): Sérsic shape parameter. Column (5): axial ratio. Column (6): major-axis position angle measured North through East. Column (7): total apparent magnitude of the Sérsic model after applying the Galactic absorption (Schlafly & Finkbeiner 2011) and K_r corrections (Chilingarian et al. 2010) available in NED. Column (8): total absolute magnitude adopting the distance modulus given in Table 1.

volving a linear combination of the stellar spectra available in the Medium Resolution Isaac Newton Telescope Library of Empirical Spectra (MILES; Sánchez-Blázquez et al. 2006; Falcón-Barroso et al. 2011) with the LOSVD in order to fit the galaxy spectrum. The optimal template spectrum and LOSVD moments were obtained by χ^2 minimization in pixel space. Before fitting, the MILES stellar spectra were logarithmically rebinned and deredshifted to rest frame. Moreover, we degraded the spectral resolution of the galaxy spectrum by convolving it with a Gaussian function in order to match the MILES spectral resolution (FWHM = 2.54 Å; Beifiori et al. 2011). In addition, we simultaneously fitted the ionized-gas emission lines detected with a S/N > 3. We

masked the bad pixels coming from imperfect subtraction of cosmic rays and sky emission lines and excluded them from the fitting procedure. We added a low-order multiplicative Legendre polynomial to correct for the different shape of the continuum in the spectra of the galaxy and optimal template due to reddening and large-scale residuals of flat-fielding and sky subtraction.

By measuring the LOSVD moments in all the available radial bins along the spatial direction we derived the radial profiles of the line-of-sight velocity v , velocity dispersion σ , third-order Gauss-Hermite moment H_3 , and fourth-order Gauss-Hermite moment H_4 of the stars. We estimated the uncertainties on the LOSVD moments running Monte

Table 3. Instrumental set up of the spectroscopic observations.

Parameter (1)	Run 1 (2)	Run 2 (3)	Run 3 (4)	Run 4 (5)
Spectrograph	Moderate resolution		Boller and Chivens	Moderate resolution
Grating (gr mm ⁻¹)	1200		600	1200
Detector name	Echelle		Echelle Ohio State University	Loral C Templeton
Detector manufacturer	SITe		Loral	SITe
Pixel number	2048 × 2048		1200 × 800	1024 × 1024
Pixel size (μm ²)	24 × 24		15 × 15	24 × 24
Gain (e ⁻ ADU ⁻¹)	2.7		2.1	3.5
Read-out noise (e ⁻ rms)	7.9		7.0	5.3
Scale (arcsec pixel ⁻¹)	0.606		0.41	0.28
Dispersion (Å pixel ⁻¹)	0.870	0.906	0.751	0.923
Slit width (arcsec)	1.9		1.7	1.9
Wavelength range (Å)	4670-6451	4675-6530	4250-5151	4700-5645
Instrumental FWHM (Å)	2.31	2.40	3.05	1.68
Instrumental σ at H β (km s ⁻¹)	60	63	80	44

Table 4. Log of the spectroscopic observations.

Galaxy (1)	Run (2)	PA (°) (3)	Position (4)	Single Exp. T. (s) (5)	Total Exp. T. (h) (6)
NGC 7113	1	0	...	3 × 3600	3.0
	3	0	...	2 × 1800	1.0
	4	90	...	6 × 3600	6.0
PGC 1852	1	-42	MJ	3 × 3600	3.0
	2	48	MN	3 × 3600	3.0
PGC 67207	1	-83	MJ	2 × 3600	2.0
	3	0	DG	2 × 1800	1.0
	4	7	MN	5 × 3600	5.0

Note. Column (1): galaxy name. Column (2): observing run. Column (3): slit position angle measured North through East. Column (4): slit position: MJ = major axis, MN = minor axis, DG = diagonal axis. Column (5): number and exposure time of the single exposures. Column (6): total exposure time.

Carlo simulations. For each radial bin we built a set of simulated galaxy spectra by randomly perturbing the best-fitting galaxy spectrum. We added to the counts of each pixel of the best-fitting galaxy spectrum a random value chosen from a Gaussian distribution with a mean of zero and the same standard deviation of the difference between the observed and best-fitting galaxy spectra in the wavelength range used in the fit and excluding the emission lines. We measured the simulated spectra as if they were real. For each LOSVD moment we adopted as error the standard deviation of the distribution of the values derived for the simulated galaxy spectra. We found no bias of the PPXF method with the adopted instrumental setups and spectral samplings in the ranges of S/N and σ which characterize the spectra of the sample galaxies. Indeed the values of H_3 and H_4 measured in a set of simulated galaxy spectra obtained by convolving the best-fitting galaxy spectrum with a Gauss-Hermite LOSVD, and adding photon, readout, and sky noise to mimic actual observations differ from the intrinsic ones only within

the estimated errors. The general trends and features of the LOSVD moments measured from the multiple observations of NGC 7113 agree within the errors.

The measured stellar kinematics are reported in Table A3 where velocities are relative to the galaxy centres. The folded kinematic profiles are plotted in the left-hand panels of Fig. 4.

4.3 Line-strength indices

We measured the Lick/IDS H β , Fe₅₂₇₀, Fe₅₃₃₅, Mgb, and Mg₂ (Faber et al. 1985; Worthey et al. 1994) and combined (Fe) (Gorgas et al. 1990) and [MgFe] (González 1993) line-strength indices. We rebinned the spectra in the dispersion direction as well in the radial one as done for measuring the stellar kinematics. We took into account for the difference between our spectral resolution and that of the Lick/IDS system (FWHM = 8.4 Å; Worthey & Ottaviani 1997) by degrading our spectra through a Gaussian convolution to match the Lick/IDS resolution before measuring the line-strength indices. We calibrated our measurements to the Lick/IDS system. To this aim, we calculated the systematic offsets to be applied to our data as the mean of the differences between the line-strength indices we measured for the available template G and K giant stars and those obtained by Worthey et al. (1994). We applied the same offsets as Wegner et al. (2012) to data obtained in runs 1 and 2. The wavelength range of run 3 brackets only the H β line-strength index. We did not apply any offset, since the H β values measured at P.A. = 0° for NGC 7113 in run 3 agree within the errors with those measured in run 1 (Fig. 4). The offsets derived in run 4 were neglected too being smaller than the mean error of the differences.

We derived the errors on the line-strength indices from photon statistics and CCD read-out noise, and we calibrated them by means of Monte Carlo simulations. The folded radial profiles of H β , [MgFe], (Fe), Mgb, and Mg₂ for all the sample galaxies are listed in Table A4 and plotted in the middle panels of Fig. 4.

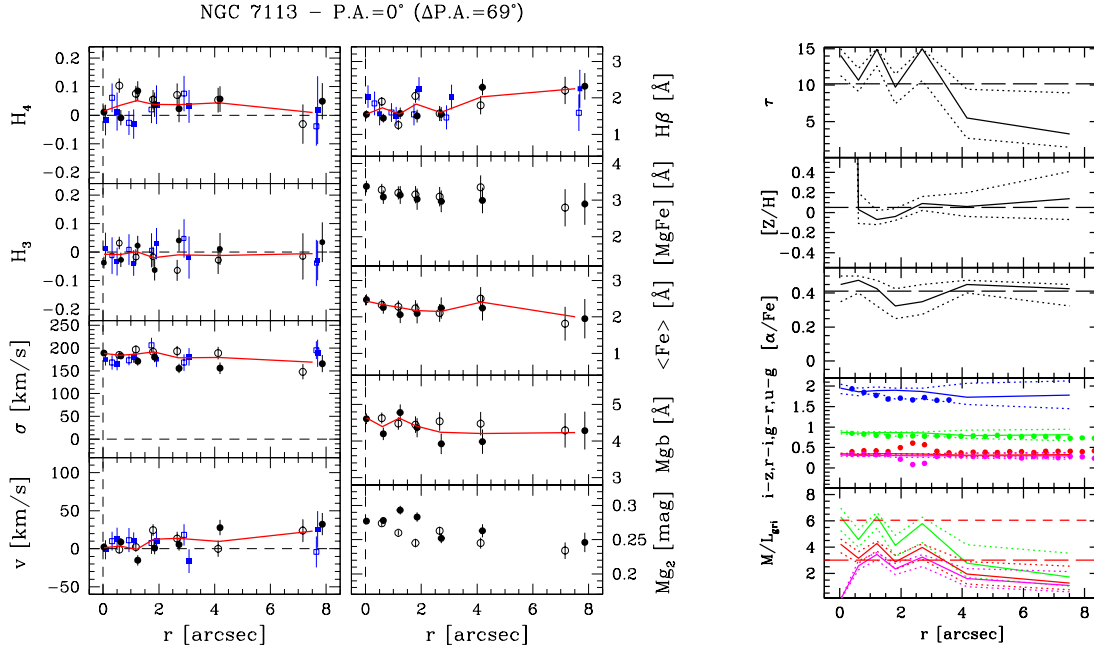


Figure 4. Folded stellar kinematics, line-strength indices, and stellar population parameters along the observed axes of the sample galaxies. Left-hand panels (from bottom to top): radial profiles of the LOS velocity (v) after the subtraction of systemic velocity, velocity dispersion (σ), third- (H_3) and fourth-order (H_4) coefficient of the Gauss-Hermite decomposition of the LOSVD. The black circles are for data measured in runs 1, 2 and 4, while blue squares are for run 3. Filled and open symbols refer to data measured along the receding and approaching side, respectively. For NGC 7113 and PGC 67207 the red solid lines correspond to the stellar kinematic parameters of the best-fitting dynamical model. The difference (Δ PA) between the PAs of the observed axis and the line of nodes adopted in the dynamical model is also given. Middle panels (from top to bottom): radial profiles of the $H\beta$, $[MgFe]$, $\langle Fe \rangle$, Mgb , and Mg_2 line-strength indices. The red solid lines correspond to the line-strength indices derived from the best-fitting SSP models with a Kroupa IMF. Symbols are the same as in the left-hand panels. Right-hand panels (from top to bottom): Radial profiles of stellar-population age (τ), metallicity ($[Z/H]$), and α -elements overabundance ($[\alpha/Fe]$) derived from the best-fitting SSP models with a Kroupa IMF with long-dashed lines marking their mean values. Below them the predicted $u-g$ (blue solid line), $g-r$ (green solid line), $r-i$ (red solid line) and $i-z$ (magenta solid line) colours are shown together with the measured ones (blue, green, red, and magenta filled circles). At the bottom, the predicted mass-to-light ratios in the g (green solid line), r (red solid line), and i (magenta solid line) band are given with the long-dashed line marking to the mean value of the mass-to-light ratio in the r -band $\Upsilon_{*,Kroupa}$. For NGC 7113 and PGC 67207, the short-dashed line corresponds to the dynamical mass-to-light ratio $\Upsilon_{*,dyn}$. The dotted lines show the error ranges for all the plotted quantities.

4.4 Properties of the stellar populations

We modelled the $H\beta$, $\langle Fe \rangle$, and Mgb line-strength indices following the method described in Saglia et al. (2010) and Pu et al. (2010). We spline interpolated the SSP models for the Kroupa IMF of Maraston (1998, 2005) on a fine grid in age ($\tau \leq 15$ Gyr on steps of 0.1 Gyr), metallicity ($-2.25 \leq [Z/H] \leq 0.67$ dex on steps of 0.02 dex), and overabundances ($-0.3 \leq [\alpha/Fe] \leq 0.5$ dex on steps of 0.05 dex). We derived at each radius the best-fitting values of τ , $[Z/H]$, and $[\alpha/Fe]$ by minimizing the difference between the values of $H\beta$, $\langle Fe \rangle$ and Mgb line-strength indices we measured in the spectra and those predicted by the SSP models for a given set of age, metallicity, and overabundance as done in Wegner et al. (2012). We took into account the measurement errors and gave the same weight to the line-strength indices to derive the best-fitting values of the stellar population properties to the same accuracy. Finally, we computed the values of the mass-to-light ratio $\Upsilon_{*,Kroupa}$ and colours $u-g$, $g-r$, $r-i$, and $i-z$ of the corresponding SSP models.

The folded radial profiles of the stellar-population age, metallicity, overabundance, and mass-to-light ratio together with the predicted and measured colour gradients are plotted in the right-hand panels of Fig. 4. The average values of τ , $[Z/H]$, $[\alpha/Fe]$, and $\Upsilon_{*,Kroupa}$ for the sample galaxies are reported in Table 5. They are in reasonable agreement with the findings of Wegner & Grogin (2008).

NGC 7113 is ~ 8 Gyr old, with metallicity slightly above solar ($[Z/H] \sim 0.2$ dex), strong overabundance ($[\alpha/Fe] \sim 0.3$ dex), and $\Upsilon_{*,Kroupa} \sim 2.5 M_{\odot}/L_{\odot}$. PGC 67207 is ~ 12 Gyr old, with sub-solar metallicity ($[Z/H] \sim -0.1$ dex), strong overabundance ($[\alpha/Fe] \sim 0.4$ dex), and $\Upsilon_{*,Kroupa} \sim 3.1 M_{\odot}/L_{\odot}$. In both cases, the predicted colour gradients of the corresponding SSP agree reasonably well with the measured ones, whereas the mass-to-light ratio of the stellar component is a factor of 2 smaller than the dynamically derived one. The barred galaxy PGC 1852 has a solar metallicity ($[Z/H] \sim 0$ dex) and strong overabundance ($[\alpha/Fe] \sim 0.4$ dex). Its age ($\tau \sim 7$ Gyr) and SSP mass-to-light ratio ($\Upsilon_{*,Kroupa} \sim 2.0 M_{\odot}/L_{\odot}$) are smaller than those of the

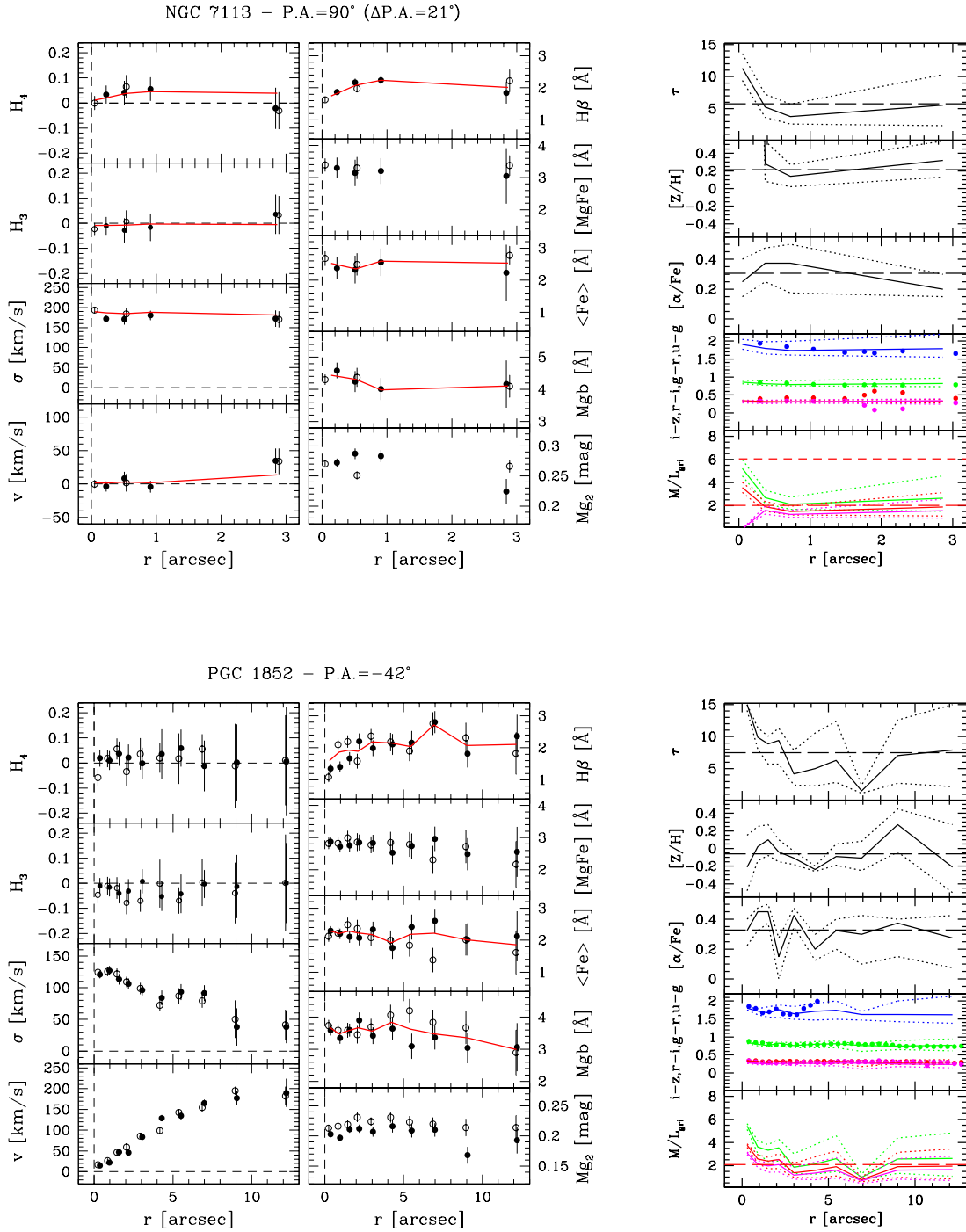


Figure 4. *continued*

other two galaxies, in agreement with the later morphological type. The older ages derived in the galactic centre could be related to the bulge component.

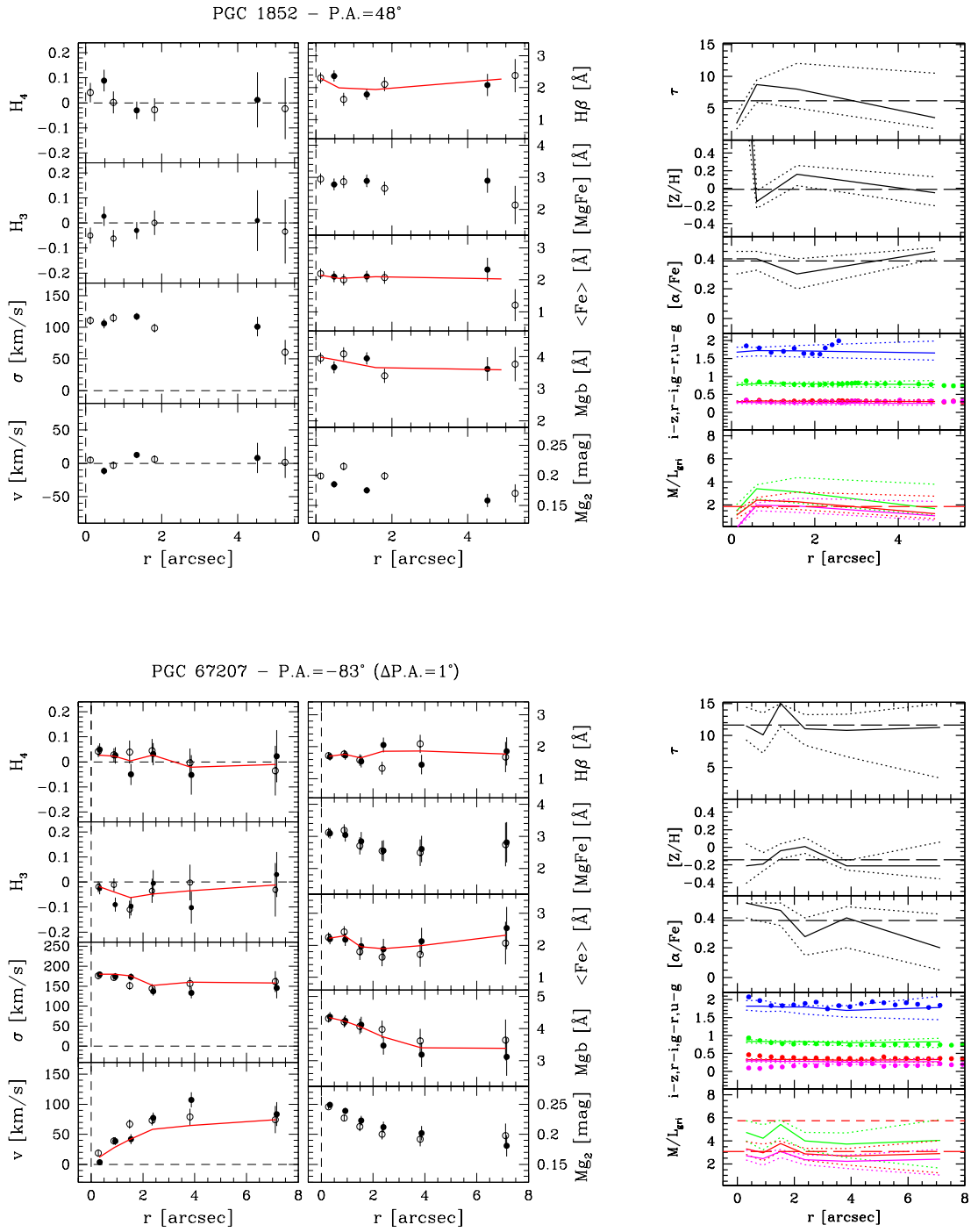


Figure 4. *continued*

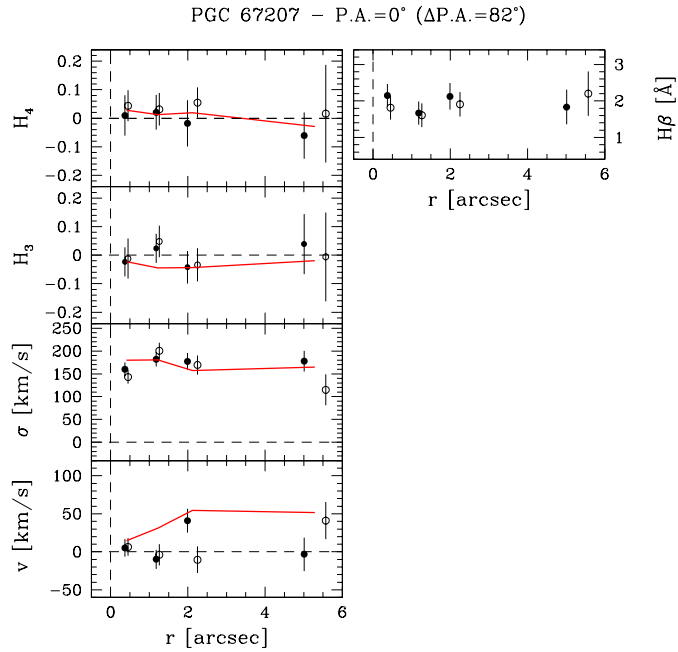
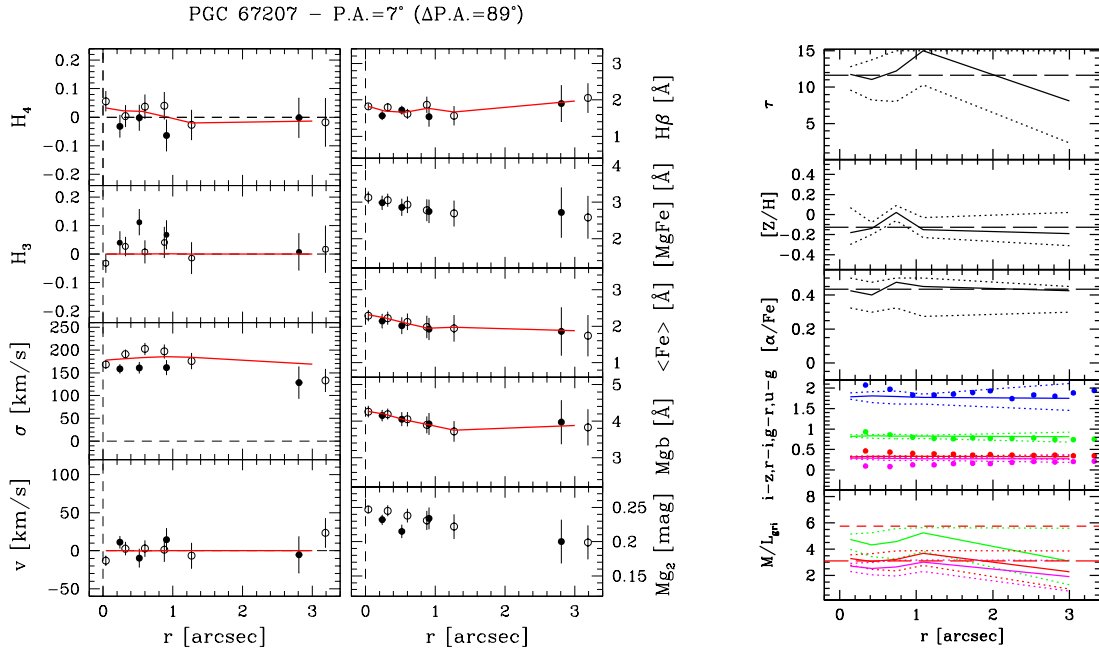


Figure 4. *continued*

Table 5. The average properties of stellar populations and DM haloes of the sample galaxies.

Galaxy	r_{eff} (kpc)	r_{enc} (kpc)	σ (km s ⁻¹)	τ (Gyr)	[Z/H] (dex)	[α /Fe] (dex)	$\Upsilon_{*,\text{Kroupa}}$ (M _⊙ /L _⊙)	$\Upsilon_{*,\text{dyn}}$ (M _⊙ /L _⊙)	$\log \langle \rho_{\text{DM,dyn}} \rangle$ (10)	$f_{\text{DM,dyn}}$ (11)	$\log \langle \rho_{\text{DM,Kroupa}} \rangle$ (12)	$f_{\text{DM,Kroupa}}$ (13)
(1)	(2)	(3)	(4)	(5)	(6)	(7)	(8)	(9)	(10)	(11)	(12)	(13)
NGC 7113	8.7	17.5	178 ± 1	8.0 ± 2.2	0.24 ± 0.08	0.30 ± 0.06	2.52 ± 0.50	7.09 ± 1.40	-1.89 ^{+0.39} _{-0.60}	0.36 ^{+0.40} _{-0.20}	-1.77 ^{+0.30} _{-0.40}	0.70 ^{+0.15} _{-0.10}
PGC 1852	95 ± 6	6.9 ± 0.6	-0.04 ± 0.06	0.36 ± 0.03	1.96 ± 0.58
PGC 67207	4.1	8.2	164 ± 5	11.6 ± 0.1	-0.13 ± 0.01	0.41 ± 0.03	3.05 ± 0.05	6.71 ± 0.85	-1.56 ^{+0.37} _{-1.10}	0.11 ^{+0.17} _{-0.10}	-1.34 ^{+0.26} _{-0.34}	0.49 ^{+0.10} _{-0.06}

Note. Column (1): name. Column (2): effective radius. Column (3): radius corresponding to $2r_{\text{eff}}$ for calculating the DM average mass density. Column (4): average velocity dispersion. Column (5): average age. Column (6): average metallicity. Column (7): average α -elements overabundance. Column (8): stellar-population mass-to-light ratio in the r band. Column (9): dynamical mass-to-light ratio of all the mass following the light in the r band. Column (10): DM-halo average mass density within r_{enc} with $\rho_{\text{DM,dyn}}$ given in M_⊙pc⁻³. Column (11): DM-halo spherically-averaged mass fraction within r_{eff} . Column (12): total DM average mass density within r_{enc} assuming a Kroupa IMF with $\rho_{\text{DM,Kroupa}}$ given in M_⊙pc⁻³. Column (13): total DM spherically-averaged mass fraction within r_{eff} assuming a Kroupa IMF.

5 DYNAMICAL MODELLING

We skipped the barred galaxy PGC 1852 and derived the mass distribution of NGC 7113 and PGC 67207 as we did for the ETGs in Coma (Thomas et al. 2007, 2011) and Abell 262 (Wegner et al. 2012) clusters. We used the axisymmetric dynamical models by Thomas et al. (2004, 2005) to obtain the mass-to-light ratio $\Upsilon_{*,\text{dyn}}$ of the mass that follows light and the structural parameters of the DM halo without assuming any particular orbit structure.

To this aim, we modelled the total mass density distribution as

$$\rho = \rho_* + \rho_{\text{DM,dyn}} = \Upsilon_{*,\text{dyn}}\nu + \frac{V_c^2}{4\pi G} \frac{3r_c^2 + r^2}{(r_c^2 + r^2)^2} \quad (4)$$

where ρ_* is the mass density of the (luminous and dark) matter that is distributed like the stars and $\rho_{\text{DM,dyn}}$ is the mass density of the DM distributed in the halo (Thomas et al. 2007; Wegner et al. 2012). We adopted a spherical cored logarithmic DM halo with asymptotically constant circular velocity V_c and constant mass density inside r_c (Binney & Tremaine 1987). We derived the radial profile of the stellar luminosity density ν by deprojecting as in Magorrian (1999) the Sérsic surface-brightness profile obtained from the photometric decomposition and by taking into account the seeing effects as in Rusli et al. (2011). We assumed both the galaxies to be seen edge on ($i = 90^\circ$). This makes the deprojection unique. We do not expect that this assumption affects our conclusions about the mass structure of the modelled galaxies, given our sparse kinematic sampling. For the same reason we do not discuss the orbital structure in detail.

Fig. 2 shows the radial profiles of the photometric parameters of NGC 7113 and PGC 67207, which we derived by projecting the deprojected stellar luminosity density without applying any correction for seeing convolution.

We computed the gravitational potential from Poisson's equation and calculated thousands of orbits in the resulting fixed potential. They were superposed to fit the observed LOSVDs with the constraint of the luminosity density and using the maximum entropy technique (Richstone & Tremaine 1988) optimized for the long-slit setup (see Thomas et al. 2004, 2005, 2007, for details).

The best-fitting mass models with a DM halo are marginally better than the ones without ($\Delta\chi^2 = 0.8$ for NGC 7113; $\Delta\chi^2 = 2$ for PGC 67207). The corresponding best-fitting kinematics are given in Fig. 4. Moreover, we computed the DM-halo average mass density $\langle\rho_{\text{DM,dyn}}\rangle$ within $r_{\text{enc}} = 2r_{\text{eff}}$ and DM-halo average mass fraction $f_{\text{DM,dyn}}$ inside r_{eff} , which we interpreted as upper limits given the low $\Delta\chi^2$ values. They are given in Table 5 together with the best-fitting $\Upsilon_{*,\text{dyn}}$ and the values of r_{eff} and r_{enc} in physical units. We opted to average the DM-halo mass density inside the larger r_{enc} to be less sensitive to slope uncertainties in the radial profile of the mass density.

Finally, we derived the total DM mass density under the assumption of Kroupa IMF as

$$\rho_{\text{DM,Kroupa}} = \rho_{\text{DM,dyn}} + (\Upsilon_{*,\text{dyn}} - \Upsilon_{*,\text{Kroupa}}) \times \nu \quad (5)$$

by summing the DM distributed in the halo and that following the light so closely that it is captured by $\Upsilon_{*,\text{dyn}}$ (Thomas et al. 2007; Wegner et al. 2012). The corresponding total DM average mass density $\langle\rho_{\text{DM,Kroupa}}\rangle$ within r_{enc}

and total DM average mass fraction $f_{\text{DM,Kroupa}}$ inside r_{eff} are reported in Table 5 too.

6 DISCUSSION AND CONCLUSIONS

Fig. 5 shows the ratio $\Upsilon_{*,\text{dyn}}/\Upsilon_{*,\text{Kroupa}}$ between the mass-to-light ratio from dynamical modelling and stellar-population analysis as a function of the velocity dispersion σ_{eff} inside r_{eff} . The values we derived for NGC 7113 and PGC 67207 are compared to those of ETGs in the SLACS (Treu et al. 2010) and ATLAS3D (Cappellari et al. 2013) surveys and in the Coma (Thomas et al. 2007, 2011) and Abell 262 (Wegner et al. 2012) clusters. The results for the ETGs studied by Spiniello et al. (2014), Conroy & van Dokkum (2012), Tortora et al. (2013), Posacki et al. (2015), Smith, Lucey, & Conroy (2015), and Leier et al. (2016) are also shown. In both the galaxies we analysed the dynamical mass following the light exceeds the Kroupa value by far ($\Upsilon_{*,\text{dyn}}/\Upsilon_{*,\text{Kroupa}} \gtrsim 2$). The trend of increasing $\Upsilon_{*,\text{dyn}}/\Upsilon_{*,\text{Kroupa}}$ with σ_{eff} is well established in ETGs (Thomas et al. 2011; Cappellari et al. 2012). It either points to a systematic variation of the IMF, from Kroupa-like in low-mass galaxies to Salpeter (or even more bottom-heavy) in most massive ones (van Dokkum & Conroy 2011; Conroy & van Dokkum 2012), or to the presence of a DM component distributed similar to the stars. Here we report large $\Upsilon_{*,\text{dyn}}/\Upsilon_{*,\text{Kroupa}}$ values for two ETGs with a relatively low velocity dispersion ($\sigma_{\text{eff}} \lesssim 170 \text{ km s}^{-1}$), where the majority of the measured galaxies so far are characterized by $1 < \Upsilon_{*,\text{dyn}}/\Upsilon_{*,\text{Kroupa}} < 1.6$ which correspond to the IMF regime between the Kroupa and Salpeter limits. We do not find any correlation between $\Upsilon_{*,\text{dyn}}/\Upsilon_{*,\text{Kroupa}}$ and the ages, metallicities, and α -element overabundance of the stellar populations like in Coma and Abell 262 ETGs, for which we made the same assumptions on mass distribution and stellar populations as in NGC 7113 and PGC 67207.

The large $\Upsilon_{*,\text{dyn}}/\Upsilon_{*,\text{Kroupa}}$ of NGC 7113 and PGC 67207 could be reduced if we had underestimated the true distances, overestimated the amount of mass following the light, and/or underestimated $\Upsilon_{*,\text{Kroupa}}$ from the stellar population analysis. Both galaxies follow within 20% the r -band Fundamental Plane of Hyde & Bernardi (2009) and this leads us to conclude that the assumed distances can not be wrong by much. Our dynamical models do include a DM halo, so it is not the assumption of self-consistency that is biasing high our $\Upsilon_{*,\text{dyn}}$ estimates (Thomas et al. 2011). In addition, using the $M_{\text{BH}} - \sigma$ relation derived by Saglia et al. (2016) we estimated the mass of the central supermassive black hole to be $M_{\text{BH}} = (0.1 - 1.4) \times 10^8 M_\odot$ for $\sigma = 170 - 180 \text{ km s}^{-1}$. The best-fitting models shown in Fig. 4 predict an enclosed mass $M(R < 1 \text{ arcsec}) \sim 7 - 8 \times 10^9 M_\odot$. So, if the masses of the supermassive black holes of the two galaxies are not severely underestimated, we do not expect a significant effect on their $\Upsilon_{*,\text{dyn}}$. But, high-resolution spectroscopy probing the black hole sphere of influence (expected to be around 0.05 arcsec) is needed to fully address this issue. Finally, NGC 7113 has a slightly supersolar metallicity and is 8 Gyr old while PGC 67297 has slightly subsolar metallicity and an age of about 12 Gyr. These are rather normal metallicities and ages for ETGs with similar velocity dispersion and we reproduced the measured $u - g$, $g - r$, $r - i$, and

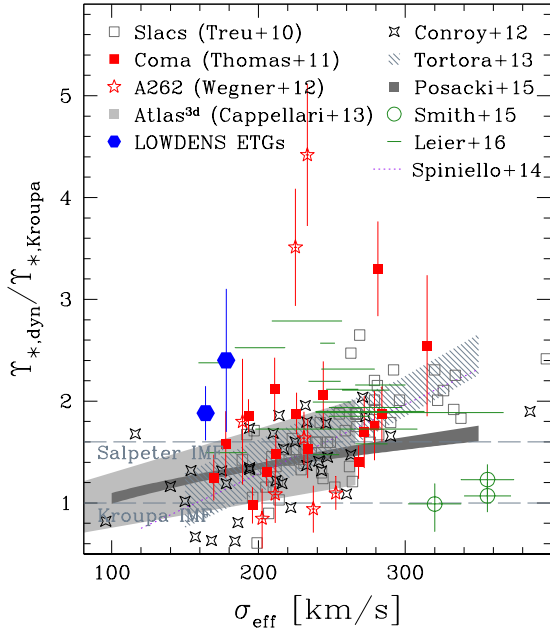


Figure 5. The $\Upsilon_{*,\text{dyn}}/\Upsilon_{*,\text{Kroupa}}$ ratio between the dynamical and stellar-population mass-to-light ratios of the ETGs NGC 7113 and PGC 67207 (blue filled hexagons) residing in low-density environments as a function of the effective velocity dispersion σ_{eff} . The values for the ETGs in the SLACS (Treu et al. 2010, open squares) and ATLAS3D (Cappellari et al. 2013, light grey region) surveys, in Coma (Thomas et al. 2011, red filled squares) and Abell 262 (Wegner et al. 2012, red open stars) clusters, and for those studied by Conroy & van Dokkum (2012, black open stars), Smith, Lucey, & Conroy (2015, green open circles) and Leier et al. (2016, green solid segments) are shown for comparison. The range of models of Tortora et al. (2013, shaded region) and the relations by Posacki et al. (2015, dark grey region) and Spiniello et al. (2014, magenta dashed line) are also given. The bottom and top horizontal dashed lines correspond to the $\Upsilon_{*,\text{dyn}}/\Upsilon_{*,\text{Kroupa}}$ values for a Kroupa and Salpeter IMF, respectively.

$i - z$ colours rather well. This means that we might have underestimated $\Upsilon_{*,\text{Kroupa}}$ by at most 20% for both galaxies.

Fig. 6 shows the average DM mass inside $2r_{\text{eff}}$ as a function of the stellar mass. Taking the dynamical mass that follows the light as the stellar mass (i.e., $M_* = \Upsilon_{*,\text{dyn}} \times L_r$), we find that the average DM-halo mass density (i.e., only due to halo DM) inside $2r_{\text{eff}}$ of NGC 7113 and PGC 67207 is higher than those of spiral galaxies (Persic et al. 1996a,b; Kormendy & Freeman 2004, 2016), but lower than the ones of cluster ETGs (Thomas et al. 2007; Wegner et al. 2012) (Fig. 6, top panel). This implies an earlier formation redshift compared to local bright spirals (Thomas et al. 2009). Moreover, the DM densities closely match the predictions of the semi-analytic models for galaxy formation in low-density regions by De Lucia & Blaizot (2007). This holds in spite of the degeneracy concerning the interpretation of $\Upsilon_{*,\text{dyn}}$, which prevents discriminating between luminous and DM once they follow close radial distributions. In fact, the agreement with theoretical predictions is even better if we assume that stellar mass is minimal by adopting a Kroupa

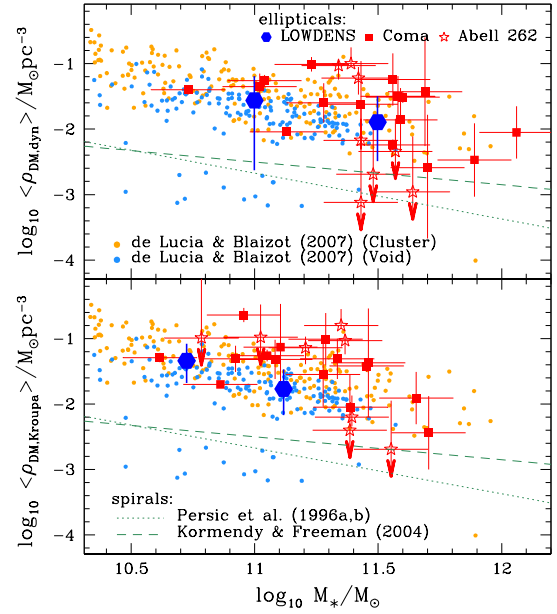


Figure 6. DM-halo average mass density (i.e., only halo DM) inside $2r_{\text{eff}}$ as a function of the mass that follows light ($M_* = \Upsilon_{*,\text{dyn}} \times L_r$, top panel) and total DM average mass density (i.e., halo DM + DM following the light) inside $2r_{\text{eff}}$ as a function of the stellar mass assuming a Kroupa IMF ($M_* = \Upsilon_{*,\text{Kroupa}} \times L_r$, bottom panel) the ETGs NGC 7113 and PGC 67207 (blue filled hexagons) residing in low-density environments and ETGs in Coma (Thomas et al. 2009, red filled squares) and Abell 262 (Wegner et al. 2012, red open stars) clusters. Predictions from semi-analytic galaxy formation models (De Lucia & Blaizot 2007) are indicated by the small yellow and cyan filled circles for high-density regions (galaxy clusters) and low-density regions (voids), respectively. The lines show spiral galaxy scaling relations from Persic et al. (1996a,b, green dotted line) and Kormendy & Freeman (2004, green dashed line; but see also Kormendy & Freeman 2016).

IMF (i.e., $M_* = \Upsilon_{*,\text{Kroupa}} \times L_r$) and consider the total DM average mass density (i.e., due to both the DM in the halo and that following the light) inside $2r_{\text{eff}}$ (Fig. 6, bottom panel). Without trying to over interpret these results given the fact the general galaxy population in voids consists of mostly small late-type spirals and massive ETGs are very rare (Croton et al. 2005; Beygu et al. 2017), the above findings suggest that DM haloes of ETGs are less dense when these objects live in low-density regions, even if more extended kinematic data are needed to confirm this, given the large errors affecting our DM densities. The same remark applies to the reported DM fractions, which are similar to the ones derived for cluster ETGs (see Table 5).

Recent studies of void galaxies (Kreckel et al. 2011, 2012; Hoyle et al. 2012; Pustilnik et al. 2013; Penny et al. 2015; Beygu et al. 2017) seem to indicate that the lower density of void regions has a smaller role on setting the galaxy properties while their nearby environments and DM haloes are more important. We presented new photometric and spectroscopic observations of three galaxies living in low-density environments. For the two of them that are

ETGs, our dynamical modelling suggests that they might have low DM content and large dynamically determined mass-to-light ratios. Further more extended (and preferably two-dimensional) stellar kinematics, combined with high-resolution spectroscopy probing the central regions and NIR measurements of the strengths of IMF-sensitive lines of these galaxies, are needed to rule out that it is not the low-density environment of these galaxies that is causing their peculiar properties.

ACKNOWLEDGMENTS

We thank the anonymous referee for constructive comments which helped us to improve this paper. We are grateful to Kathryn Kreckel for providing us the filtered density contrast of the galaxies from Grogin & Geller (1999) and to Margaret Geller for valuable discussion. EMC was supported by Padua University through grants 60A02-5857/13, 60A02-5833/14, 60A02-4434/15, CPDA133894, and BIRD164402/16. EMC acknowledges the Max-Planck-Institut für extraterrestrische Physik for the hospitality while this paper was in progress. This investigation was based on observations obtained at the Michigan-Dartmouth-MIT (MDM) Observatory and at the Gemini Observatory under program GN-2011B-9-80. MDM Observatory, Kitt Peak, Arizona is operated by a consortium of Dartmouth College, the University of Michigan, Columbia University, the Ohio State University, and Ohio University. Gemini Observatory is operated by the Association of Universities for Research in Astronomy, Inc., under a cooperative agreement with the NSF on behalf of the Gemini partnership: the National Science Foundation (United States), the National Research Council (Canada), CONICYT (Chile), Ministerio de Ciencia, Tecnología e Innovación Productiva (Argentina), and Ministério da Ciência, Tecnologia e Inovação (Brazil). Parts of the data used in this research were acquired through the Sloan Digital Sky Survey (SDSS) Archive (<http://www.sdss.org/>). Funding for the creation and distribution of the SDSS Archive has been provided by the Alfred P. Sloan Foundation, the Participating Institutions, the National Aeronautics and Space Administration, the National Science Foundation, the US Department of Energy, the Japanese Monbukagakusho, and the Max Planck Society. The SDSS is managed by the Astrophysical Research Consortium (ARC) for the Participating Institutions. The Participating Institutions are The University of Chicago, Fermilab, the Institute for Advanced Study, the Japan Participation Group, The Johns Hopkins University, the Korean Scientist Group, Los Alamos National Laboratory, the Max-Planck-Institute for Astronomy (MPIA), the Max-Planck-Institute for Astrophysics (MPA), New Mexico State University, University of Pittsburgh, University of Portsmouth, Princeton University, the United States Naval Observatory, and the University of Washington. This research also made use of the HyperLeda Database (<http://leda.univ-lyon1.fr/>) and NASA/IPAC Extragalactic Database (NED) which is operated by the Jet Propulsion Laboratory, California Institute of Technology, under contract with the National Aeronautics and Space Administration (<http://ned.ipac.caltech.edu/>).

REFERENCES

- Abazajian K. N., et al., 2009, *ApJS*, 182, 543
 Ahn C. P. et al., 2012, *ApJS*, 203, 21
 Auger M. W., Treu T., Gavazzi R., Bolton A. S., Koopmans L. V. E., Marshall P. J., 2010, *ApJ*, 721, L163
 Barnabè M., Spiniello C., Koopmans L. V. E., Trager S. C., Czoske O., Treu T., 2013, *MNRAS*, 436, 253
 Beifiori A., Maraston C., Thomas D., Johansson J., 2011, *A&A*, 531, A109
 Bender R., Moellenhoff C., 1987, *A&A*, 177, 71
 Bernardi M., Renzini A., da Costa L. N., Wegner G., Alonso M. V., Pellegrini P. S., Rit e C., Willmer C. N. A., 1998, *ApJ*, 508, L143
 Bernardi M., Shankar F., Hyde J. B., Mei S., Marulli F., Sheth R. K., 2010, *MNRAS*, 404, 2087
 Beygu B., Peletier R. F., van der Hulst J. M., Jarrett T. H., Kreckel K., van de Weygaert R., van Gorkom J. H., Aragon-Calvo M. A., 2017, *MNRAS*, 464, 666
 Binney J., Tremaine S., 1987, *Galactic Dynamics*. Princeton Univ. Press, Princeton, NJ
 Boccas M. et al., 2006, *Proc. SPIE*, 6272, 62723L
 Cappellari M. et al., 2006, *MNRAS*, 366, 1126
 Cappellari M., Emsellem E., 2004, *PASP*, 116, 138
 Cappellari M., et al. 2012, *Nature*, 484, 485
 Cappellari M. et al., 2013, *MNRAS*, 432, 1709
 Chilingarian I. V., Melchior A.-L., Zolotukhin I. Y., 2010, *MNRAS*, 405, 1409
 Christou J. C. et al., 2010, *Proc. SPIE*, 7736, 77361R
 Ciotti L., 1991, *A&A*, 249, 99
 Colberg J. M., et al., 2008, *MNRAS*, 387, 933
 Conroy C., van Dokkum P. G., 2012, *ApJ*, 760, 71
 Corsini E. M., Wegner G., Saglia R. P., Thomas J., Bender R., Thomas D., 2008, *ApJS*, 175, 462
 Croton D. J., Farrar G. R., 2008, *MNRAS*, 386, 2285
 Croton D. J., et al., 2005, *MNRAS*, 356, 1155
 Daddi E. et al., 2005, *ApJ*, 626, 680
 De Lucia G., Blaizot J., 2007, *MNRAS*, 375, 2
 Dutton A. A., Macci o A. V., Mendel J. T., Simard L., 2013, *MNRAS*, 432, 2496
 Faber S. M., Friel E. D., Burstein D., Gaskell C. M., 1985, *ApJS*, 57, 711
 Falc n-Barroso J., S nchez-Bl zquez P., Vazdekis A., Ricciardelli E., Cardiel N., Cenarro A. J., Gorgas J., Peletier R. F., 2011, *A&A*, 532, A95
 Ferreras I., La Barbera F., de la Rosa I. G., Vazdekis A., de Carvalho R. R., Falc n-Barroso J., Ricciardelli E., 2013, *MNRAS*, 429, L15
 Fraser-McKelvie A., Pimblet K. A., Penny S. J., Brown M. J. I., 2016, *MNRAS*, 459, 754
 Fukugita M., Hogan C. J., Peebles P. J. E., 1998, *ApJ*, 503, 518
 Geller M. J., Huchra J. P., 1989, *Science*, 246, 897
 Gerhard O. E., 1993, *MNRAS*, 265, 213
 Gnedin O. Y., Kravtsov A. V., Klypin A. A., Nagai D., 2004, *ApJ*, 616, 16
 Gonz lez J. J., 1993, PhD thesis, Univ. California
 Gorgas J., Efstathiou G., Aragon Salamanca A., 1990, *MNRAS*, 245, 217
 Grogin N. A., Geller M. J., 1999, *AJ*, 118, 2561
 Hahn O., Carollo C. M., Porciani C., Dekel A., 2007, *MNRAS*, 381, 41

- Hilz M., Naab T., Ostriker J. P., Thomas J., Burkert A., Jesseit R., 2012, *MNRAS*, 425, 3119
- Hodapp K. W. et al., 2003, *PASP*, 115, 1388
- Hoyle F., Vogeley M. S., Pan D., 2012, *MNRAS*, 426, 3041
- Hyde J. B., Bernardi M., 2009, *MNRAS*, 396, 1171
- Kauffmann G., White S. D. M., Heckman T. M., Ménard B., Brinchmann J., Charlot S., Tremonti C., Brinkmann J., 2004, *MNRAS*, 353, 713
- Kormendy J., Freeman K. C., 2004, in Ryder S., Pisano D., Walker M., Freeman K., eds, *Proc. IAU Symp. 220, Dark Matter in Galaxies*. Astron. Soc. Pac., San Francisco, p. 377
- Kormendy J., Freeman K. C., 2016, *ApJ*, 817, 84
- Kreckel K., Platen E., Aragón-Calvo M. A., van Gorkom J. H., van de Weygaert R., van der Hulst J. M., Beygu B., 2012, *AJ*, 144, 16
- Kreckel K. et al., 2011, *AJ*, 141, 4
- La Barbera F., Ferreras I., Vazdekis A., de la Rosa I. G., de Carvalho R. R., Trevisan M., Falcón-Barroso J., Ricciardelli E., 2013, *MNRAS*, 433, 3017
- Leier D., Ferreras I., Saha P., Charlot S., Bruzual G., La Barbera F., 2016, *MNRAS*, 459, 3677
- Magorrian J., 1999, *MNRAS*, 302, 530
- Maraston C., 1998, *MNRAS*, 300, 872
- Maraston C., 2005, *MNRAS*, 362, 799
- Martín-Navarro I., Barbera F. L., Vazdekis A., Falcón-Barroso J., Ferreras I., 2015, *MNRAS*, 447, 1033
- Mehlert D., Saglia R. P., Bender R., Wegner G., 2000, *A&AS*, 141, 449
- Méndez-Abreu J., Aguerri J. A. L., Corsini E. M., Simonneau E., 2008, *A&A*, 478, 353
- Méndez-Abreu J., Debattista V. P., Corsini E. M., Aguerri J. A. L., 2014, *A&A*, 572, A25
- Moffat A. F. J., 1969, *A&A*, 3, 455
- Osterbrock D. E., Fulbright J. P., Martel A. R., Keane M. J., Trager S. C., Basri G., 1996, *PASP*, 108, 277
- Padmanabhan N. et al., 2008, *ApJ*, 674, 1217
- Penny S. J., et al., 2015, *MNRAS*, 453, 3519
- Persic M., Salucci P., Stel F., 1996a, *MNRAS*, 281, 27
- Persic M., Salucci P., Stel F., 1996b, *MNRAS*, 283, 1102
- Posacki S., Cappellari M., Treu T., Pellegrini S., Ciotti L., 2015, *MNRAS*, 446, 493
- Pu S. B., Saglia R. P., Fabricius M. H., Thomas J., Bender R., Han Z., 2010, *A&A*, 516, A4
- Pustilnik S. A., Martin J.-M., Lyamina Y. A., Kniazev A. Y., 2013, *MNRAS*, 432, 2224
- Richstone D. O., Tremaine S., 1988, *ApJ*, 327, 82
- Rieder S., van de Weygaert R., Cautun M., Beygu B., Portegies Zwart S., 2013, *MNRAS*, 435, 222
- Rusli S. P., Thomas J., Erwin P., Saglia R. P., Nowak N., Bender R., 2011, *MNRAS*, 410, 1223
- Saglia R. P. et al., 2010, *A&A*, 509, A61
- Saglia R. P. et al., 2016, *ApJ*, 818, 47
- Sánchez-Blázquez P. et al., 2006, *MNRAS*, 371, 703
- Sarzi M. et al., 2006, *MNRAS*, 366, 1151
- Schlafly E. F., Finkbeiner D. P., 2011, *ApJ*, 737, 103
- Sérsic J. L., 1968, *Atlas de Galaxias Australes*. Observatorio Astronómico de Córdoba, Córdoba
- Smith R. J., Lucey J. R., Conroy C., 2015a, *MNRAS*, 449, 3441
- Smith R. J., Alton P., Lucey J. R., Conroy C., Carter D., 2015b, *MNRAS*, 454, L71
- Spiniello C., Trager S. C., Koopmans L. V. E., Chen Y. P., 2012, *ApJ*, 753, L32
- Spiniello C., Trager S., Koopmans L. V. E., Conroy C., 2014, *MNRAS*, 438, 1483
- Thomas J., Saglia R. P., Bender R., Erwin P., Fabricius M., 2014, *ApJ*, 782, 39
- Thomas J., Saglia R. P., Bender R., Thomas D., Gebhardt K., Magorrian J., Corsini E. M., Wegner G., 2005, *MNRAS*, 360, 1355
- Thomas J., Saglia R. P., Bender R., Thomas D., Gebhardt K., Magorrian J., Corsini E. M., Wegner G., 2007, *MNRAS*, 382, 657
- Thomas J., Saglia R. P., Bender R., Thomas D., Gebhardt K., Magorrian J., Corsini E. M., Wegner G., 2009, *ApJ*, 691, 770
- Thomas J. et al., 2011, *MNRAS*, 415, 545
- Thomas J., Saglia R. P., Bender R., Thomas D., Gebhardt K., Magorrian J., Richstone D., 2004, *MNRAS*, 353, 391
- Tortora C., Romanowsky A. J., Napolitano N. R., 2013, *ApJ*, 765, 8
- Treu T., Auger M. W., Koopmans L. V. E., Gavazzi R., Marshall P. J., Bolton A. S., 2010, *ApJ*, 709, 1195
- van der Marel R. P., Franx M., 1993, *ApJ*, 407, 525
- van Dokkum P. G., 2001, *PASP*, 113, 1420
- van Dokkum P. G., Conroy C., 2010, *Nature*, 468, 940
- van Dokkum P. G., Conroy C., 2011, *ApJ*, 735, L13
- Wechsler R. H., Bullock J. S., Primack J. R., Kravtsov A. V., Dekel A., 2002, *ApJ*, 568, 52
- Wegner G., Corsini E. M., Saglia R. P., Bender R., Merkl D., Thomas D., Thomas J., Mehlert D., 2002, *A&A*, 395, 753
- Wegner G., Grogin N. A., 2008, *AJ*, 136, 1
- Wegner G. A., Corsini E. M., Thomas J., Saglia R. P., Bender R., Pu S. B., 2012, *AJ*, 144, 78
- Worthey G., Faber S. M., Gonzalez J. J., Burstein D., 1994, *ApJS*, 94, 687
- Worthey G., Ottaviani D. L., 1997, *ApJS*, 111, 377

APPENDIX A: DATA TABLES

Please note: Oxford University Press is not responsible for the content or functionality of any supporting materials supplied by the authors. Any queries (other than missing material) should be directed to the corresponding author for the article.

Table A1. Photometric parameters of the sample galaxies from SDSS data.

a (arcsec) (1)	μ_r (mag arcsec ⁻²) (2)	e (3)	PA (°) (4)	Δx_c (arcsec) (5)	Δy_c (arcsec) (6)	Err. (arcsec) (7)	a_3/a ×100 (8)	b_3/a ×100 (9)	a_4/a ×100 (10)	b_4/a ×100 (11)	a_6/a ×100 (12)	b_6/a ×100 (13)	Err. (14)
NGC 7113													
0.207 ± 0.049	17.181 ± 0.012	0.074 ± 0.310	83.23 ± 129.73	0.000	0.000	0.014	-0.33	-1.10	-4.24	0.57	0.79	0.28	1.57
0.327 ± 0.083	17.230 ± 0.013	0.082 ± 0.330	83.07 ± 125.43	-0.008	-0.008	0.023	-0.39	-1.39	-4.91	0.60	0.38	0.25	1.63
0.437 ± 0.023	17.214 ± 0.013	0.073 ± 0.069	84.09 ± 29.29	-0.012	-0.008	0.007	-0.52	-0.91	-4.77	0.89	0.78	-0.19	0.80
0.500 ± 0.011	17.415 ± 0.014	0.050 ± 0.029	80.99 ± 17.56	-0.012	-0.008	0.003	-0.15	-0.43	-2.40	-0.04	0.26	0.11	0.38
0.557 ± 0.008	17.465 ± 0.014	0.048 ± 0.019	79.59 ± 11.96	-0.012	-0.008	0.002	-0.06	-0.18	-1.75	-0.19	0.16	0.19	0.24

Note. A machine-readable version of the full table is available online. A few rows of the table are given for showing purpose. Column (1): semimajor axis. Column (2): azimuthally averaged r -band surface brightness. Column (3): ellipticity defined as $e = 1 - b/a$ with b semiminor axis. Column (4): major-axis position angle measured North through East. Column (5): x -coordinate of the centre. Column (6): y -coordinate of the centre. Column (7): Error on the centre coordinates defined as $\text{Err} = \text{rms}_{\text{fit}}/\sqrt{N}$ and derived from the residual standard deviation rms_{fit} of the ellipse fit to the $N \leq 128$ points of the isophote. Column (8): third-order sine Fourier coefficient. Column (9): third-order cosine Fourier coefficient. Column (10): fourth-order sine Fourier coefficient. Column (11): fourth-order cosine Fourier coefficient. Column (12): sixth-order sine Fourier coefficient. Column (13): sixth-order cosine Fourier coefficient. Column (14): error of Fourier coefficients defined as $\text{Err} = \sqrt{\frac{\sum_{i=10}^{N/2} (a_i^2 + b_i^2)}{N/2 - 10}} \times \frac{100}{a}$.

Table A2. Photometric parameters of the sample galaxies from Gemini data.

NGC 7113		PGC 67207	
a	μ_r	a	μ_r
(arcsec)	(mag arcsec ⁻²)	(arcsec)	(mag arcsec ⁻²)
(1)	(2)	(3)	(4)
0.007 ± 0.001	15.915 ± 0.010	0.007 ± 0.001	15.204 ± 0.010
0.080 ± 0.001	16.043 ± 0.004	0.030 ± 0.001	15.329 ± 0.009
0.152 ± 0.001	16.195 ± 0.003	0.086 ± 0.001	15.490 ± 0.008
0.184 ± 0.001	16.320 ± 0.002	0.100 ± 0.001	15.619 ± 0.007
0.216 ± 0.001	16.420 ± 0.002	0.116 ± 0.002	15.709 ± 0.007
0.248 ± 0.001	16.519 ± 0.002	0.132 ± 0.002	15.808 ± 0.007
0.283 ± 0.001	16.621 ± 0.002	0.148 ± 0.001	15.920 ± 0.007
0.321 ± 0.001	16.723 ± 0.002	0.165 ± 0.001	16.025 ± 0.005
0.359 ± 0.001	16.824 ± 0.002	0.186 ± 0.002	16.126 ± 0.005
0.401 ± 0.001	16.924 ± 0.001	0.211 ± 0.002	16.225 ± 0.005
0.443 ± 0.001	17.025 ± 0.001	0.240 ± 0.002	16.333 ± 0.005
0.488 ± 0.001	17.127 ± 0.001	0.270 ± 0.002	16.437 ± 0.005
0.540 ± 0.001	17.227 ± 0.001	0.302 ± 0.002	16.540 ± 0.004
0.595 ± 0.001	17.328 ± 0.001	0.335 ± 0.002	16.643 ± 0.003
0.649 ± 0.001	17.431 ± 0.001	0.380 ± 0.002	16.749 ± 0.003
0.713 ± 0.002	17.530 ± 0.001	0.425 ± 0.002	16.854 ± 0.003
0.776 ± 0.002	17.631 ± 0.001	0.468 ± 0.002	16.960 ± 0.003
0.845 ± 0.002	17.733 ± 0.001	0.516 ± 0.002	17.068 ± 0.002
0.915 ± 0.002	17.834 ± 0.001	0.563 ± 0.002	17.175 ± 0.002
1.000 ± 0.001	17.939 ± 0.001	0.622 ± 0.002	17.282 ± 0.002
1.088 ± 0.001	18.043 ± 0.001	0.679 ± 0.002	17.389 ± 0.002
1.181 ± 0.002	18.145 ± 0.001	0.741 ± 0.003	17.500 ± 0.002
1.281 ± 0.002	18.249 ± 0.001	0.807 ± 0.003	17.611 ± 0.002
1.392 ± 0.003	18.352 ± 0.001	0.877 ± 0.004	17.724 ± 0.002
1.522 ± 0.003	18.455 ± 0.001	0.959 ± 0.004	17.840 ± 0.002
1.648 ± 0.003	18.560 ± 0.001	1.044 ± 0.004	17.959 ± 0.002
1.795 ± 0.004	18.665 ± 0.001	1.137 ± 0.004	18.075 ± 0.002
1.958 ± 0.004	18.770 ± 0.001	1.240 ± 0.004	18.196 ± 0.002
2.144 ± 0.006	18.876 ± 0.001	1.356 ± 0.005	18.319 ± 0.002
2.348 ± 0.007	18.980 ± 0.001	1.484 ± 0.005	18.442 ± 0.001
2.576 ± 0.007	19.086 ± 0.001	1.631 ± 0.007	18.571 ± 0.001
2.795 ± 0.008	19.192 ± 0.001	1.792 ± 0.008	18.704 ± 0.001
3.032 ± 0.009	19.298 ± 0.001	1.974 ± 0.010	18.840 ± 0.001
3.276 ± 0.010	19.410 ± 0.001	2.213 ± 0.012	18.979 ± 0.001
3.535 ± 0.013	19.520 ± 0.001	2.469 ± 0.014	19.123 ± 0.001
3.806 ± 0.016	19.630 ± 0.001	2.752 ± 0.016	19.272 ± 0.001
4.084 ± 0.016	19.741 ± 0.001	3.069 ± 0.018	19.430 ± 0.001
4.381 ± 0.018	19.853 ± 0.001	3.394 ± 0.022	19.592 ± 0.001
4.709 ± 0.021	19.971 ± 0.001	3.766 ± 0.023	19.758 ± 0.001
5.056 ± 0.025	20.088 ± 0.001
5.457 ± 0.027	20.208 ± 0.001
5.859 ± 0.031	20.326 ± 0.001
6.335 ± 0.031	20.445 ± 0.001
6.829 ± 0.038	20.572 ± 0.001

Note. Columns (1) and (3): semimajor axis. Columns (2) and (4): azimuthally averaged r -band surface brightness.

Table A3. Stellar kinematics of the sample galaxies.

r (arcsec) (1)	V (km s ⁻¹) (2)	σ (km s ⁻¹) (3)	H_3 (4)	H_4 (5)	PA (°) (6)	Run (7)
NGC 7113						
-7.86	32.4 ± 14.6	165.6 ± 18.8	0.035 ± 0.070	0.049 ± 0.064	0	1
-4.19	27.9 ± 10.0	155.6 ± 12.9	0.011 ± 0.056	0.057 ± 0.045	0	1
-2.72	5.6 ± 7.8	155.4 ± 10.2	0.041 ± 0.038	0.023 ± 0.048	0	1
-1.85	1.2 ± 8.5	179.8 ± 10.9	-0.063 ± 0.036	0.037 ± 0.043	0	1
-1.24	-15.2 ± 6.8	170.8 ± 9.5	0.023 ± 0.034	0.085 ± 0.034	0	1
-0.64	8.8 ± 5.3	182.9 ± 6.3	-0.027 ± 0.025	-0.009 ± 0.027	0	1
-0.03	2.4 ± 4.6	188.9 ± 5.8	-0.037 ± 0.021	0.011 ± 0.024	0	1
0.58	1.1 ± 4.7	184.5 ± 7.0	-0.032 ± 0.022	0.104 ± 0.025	0	1
1.18	-2.2 ± 6.1	196.7 ± 8.2	0.017 ± 0.027	0.075 ± 0.028	0	1
1.79	-24.5 ± 7.6	191.4 ± 10.0	0.016 ± 0.035	0.055 ± 0.034	0	1
2.66	-13.5 ± 8.8	193.1 ± 11.7	0.064 ± 0.037	0.071 ± 0.040	0	1
4.13	-0.0 ± 10.7	189.0 ± 13.7	0.028 ± 0.048	0.053 ± 0.043	0	1
7.16	-23.9 ± 14.5	147.9 ± 16.3	0.015 ± 0.080	-0.031 ± 0.068	0	1
-7.65	4.1 ± 20.5	195.1 ± 19.6	0.038 ± 0.081	-0.039 ± 0.068	0	3
-2.90	-18.3 ± 13.9	168.0 ± 18.4	-0.048 ± 0.068	0.076 ± 0.062	0	3
-1.74	-7.5 ± 14.2	206.2 ± 16.3	-0.006 ± 0.060	0.020 ± 0.048	0	3
-0.93	-11.4 ± 15.9	173.0 ± 10.9	-0.009 ± 0.054	-0.027 ± 0.042	0	3
-0.32	-10.1 ± 12.2	168.3 ± 15.8	0.012 ± 0.064	0.061 ± 0.050	0	3
0.09	-1.2 ± 12.4	174.7 ± 13.1	0.013 ± 0.055	-0.017 ± 0.054	0	3
0.50	13.1 ± 14.6	165.6 ± 14.8	-0.033 ± 0.049	0.013 ± 0.067	0	3
1.10	11.1 ± 10.6	179.3 ± 11.6	-0.038 ± 0.045	-0.031 ± 0.052	0	3
1.92	11.0 ± 13.6	175.4 ± 17.0	0.030 ± 0.055	0.037 ± 0.068	0	3
3.08	-16.2 ± 15.5	180.6 ± 19.0	-0.019 ± 0.074	0.031 ± 0.058	0	3
7.69	25.5 ± 24.1	188.3 ± 29.7	-0.029 ± 0.069	0.018 ± 0.119	0	3
-2.84	34.9 ± 18.2	172.4 ± 20.3	0.036 ± 0.078	-0.021 ± 0.082	90	5
-0.91	-4.1 ± 8.3	180.3 ± 11.2	-0.016 ± 0.054	0.056 ± 0.046	90	5
-0.51	8.4 ± 10.0	170.7 ± 13.5	-0.028 ± 0.048	0.041 ± 0.048	90	5
-0.23	-3.6 ± 7.5	171.8 ± 9.4	-0.010 ± 0.036	0.034 ± 0.036	90	5
0.05	0.1 ± 5.5	193.7 ± 6.5	0.023 ± 0.023	0.000 ± 0.027	90	5
0.54	-1.8 ± 13.2	183.9 ± 14.5	-0.007 ± 0.045	0.065 ± 0.047	90	5
2.89	-33.8 ± 19.4	170.5 ± 20.1	-0.033 ± 0.076	-0.031 ± 0.074	90	5
PGC 1852						
-12.14	-182.4 ± 22.3	41.4 ± 24.1	-0.002 ± 0.193	0.011 ± 0.180	-42	1
-8.95	-194.9 ± 9.6	50.4 ± 29.9	0.039 ± 0.121	-0.011 ± 0.167	-42	1
-6.86	-154.5 ± 9.1	79.4 ± 10.8	-0.003 ± 0.094	0.056 ± 0.059	-42	1
-5.38	-142.8 ± 7.6	87.2 ± 12.1	0.069 ± 0.053	0.017 ± 0.101	-42	1
-4.17	-98.6 ± 8.6	72.3 ± 9.7	0.001 ± 0.096	0.020 ± 0.059	-42	1
-2.94	-85.8 ± 6.2	98.9 ± 9.0	0.070 ± 0.044	0.036 ± 0.063	-42	1
-2.06	-58.9 ± 9.5	109.3 ± 8.2	0.078 ± 0.046	-0.034 ± 0.059	-42	1
-1.45	-46.2 ± 6.4	121.8 ± 8.9	0.019 ± 0.043	0.056 ± 0.042	-42	1
-0.85	-26.3 ± 5.3	125.6 ± 7.0	0.010 ± 0.036	0.018 ± 0.035	-42	1
-0.24	-16.9 ± 5.0	124.6 ± 5.5	0.046 ± 0.034	-0.058 ± 0.034	-42	1
0.37	14.4 ± 4.7	120.8 ± 6.1	-0.010 ± 0.031	0.019 ± 0.034	-42	1
0.97	21.8 ± 5.5	127.2 ± 7.0	-0.016 ± 0.035	0.010 ± 0.037	-42	1
1.58	46.9 ± 6.3	113.5 ± 8.0	-0.040 ± 0.039	0.037 ± 0.047	-42	1
2.18	45.8 ± 7.1	106.3 ± 8.7	-0.031 ± 0.048	0.022 ± 0.052	-42	1
3.06	83.3 ± 6.5	96.3 ± 8.4	0.008 ± 0.048	-0.001 ± 0.062	-42	1
4.29	128.9 ± 7.8	84.0 ± 11.7	-0.053 ± 0.058	0.036 ± 0.099	-42	1
5.51	134.3 ± 9.5	93.4 ± 12.6	-0.042 ± 0.077	0.059 ± 0.074	-42	1
6.99	165.0 ± 8.1	91.4 ± 12.2	-0.003 ± 0.055	-0.012 ± 0.100	-42	1
9.06	177.3 ± 17.1	38.0 ± 29.5	-0.013 ± 0.126	0.002 ± 0.152	-42	1
12.20	189.7 ± 34.1	37.9 ± 25.3	0.001 ± 0.160	0.005 ± 0.217	-42	1
-5.25	-1.4 ± 23.0	60.7 ± 19.0	0.034 ± 0.127	-0.023 ± 0.121	48	2
-1.81	-5.9 ± 5.8	98.7 ± 6.9	-0.001 ± 0.049	-0.028 ± 0.046	48	2
-0.73	3.2 ± 5.2	114.9 ± 7.1	0.062 ± 0.034	0.002 ± 0.044	48	2

Table A3 – continued

−0.12	−4.8 ± 4.7	110.8 ± 6.5	0.050 ± 0.032	0.041 ± 0.039	48	2
0.48	−11.5 ± 5.3	106.1 ± 7.7	0.027 ± 0.039	0.089 ± 0.043	48	2
1.34	12.4 ± 4.8	117.2 ± 5.7	−0.030 ± 0.034	−0.030 ± 0.035	48	2
4.52	7.9 ± 22.2	101.1 ± 15.0	0.010 ± 0.120	0.012 ± 0.109	48	2
PGC 1852						
−7.16	83.5 ± 19.4	145.3 ± 25.2	0.030 ± 0.089	0.023 ± 0.103	−83	1
−3.87	107.3 ± 12.6	133.5 ± 13.8	−0.102 ± 0.064	−0.052 ± 0.079	−83	1
−2.40	77.3 ± 8.7	137.0 ± 10.7	−0.005 ± 0.053	0.031 ± 0.044	−83	1
−1.54	41.7 ± 8.2	172.9 ± 8.9	−0.097 ± 0.037	−0.050 ± 0.042	−83	1
−0.93	38.5 ± 5.9	174.5 ± 7.7	−0.090 ± 0.027	0.026 ± 0.032	−83	1
−0.33	3.6 ± 4.8	179.0 ± 6.4	−0.026 ± 0.023	0.049 ± 0.025	−83	1
0.28	−18.9 ± 4.3	176.1 ± 5.7	0.019 ± 0.021	0.042 ± 0.023	−83	1
0.88	−39.0 ± 5.1	171.9 ± 6.6	0.011 ± 0.026	0.028 ± 0.027	−83	1
1.49	−67.3 ± 7.3	151.2 ± 9.2	0.110 ± 0.035	0.039 ± 0.045	−83	1
2.35	−73.3 ± 8.3	143.9 ± 11.1	0.035 ± 0.048	0.045 ± 0.047	−83	1
3.82	−79.2 ± 13.4	156.8 ± 15.6	0.002 ± 0.071	−0.004 ± 0.057	−83	1
7.11	−74.6 ± 22.8	161.4 ± 26.2	0.031 ± 0.107	−0.035 ± 0.099	−83	1
−5.57	−41.1 ± 24.3	115.1 ± 34.0	0.006 ± 0.156	0.016 ± 0.171	0	3
−2.25	10.4 ± 17.5	169.3 ± 20.7	0.034 ± 0.058	0.055 ± 0.053	0	3
−1.26	4.0 ± 14.1	200.4 ± 17.7	−0.048 ± 0.055	0.031 ± 0.057	0	3
−0.45	−6.3 ± 11.5	143.2 ± 14.9	0.012 ± 0.070	0.044 ± 0.054	0	3
0.37	5.2 ± 11.5	159.9 ± 15.3	−0.023 ± 0.051	0.010 ± 0.071	0	3
1.18	−9.8 ± 12.6	182.0 ± 15.8	0.024 ± 0.051	0.021 ± 0.061	0	3
1.99	40.9 ± 15.5	177.4 ± 18.3	−0.042 ± 0.057	−0.018 ± 0.081	0	3
5.01	−3.2 ± 22.0	177.8 ± 22.7	0.039 ± 0.105	−0.061 ± 0.081	0	3
−2.81	−5.3 ± 24.0	128.6 ± 35.0	0.008 ± 0.065	−0.002 ± 0.070	7	5
−0.91	14.6 ± 15.3	161.5 ± 16.4	0.068 ± 0.051	−0.064 ± 0.056	7	5
−0.52	−9.6 ± 12.4	160.9 ± 12.6	0.112 ± 0.046	−0.002 ± 0.046	7	5
−0.24	11.2 ± 8.2	158.6 ± 10.0	0.040 ± 0.040	−0.032 ± 0.040	7	5
0.04	13.1 ± 6.8	168.2 ± 9.2	0.032 ± 0.033	0.056 ± 0.036	7	5
0.32	−2.9 ± 8.4	191.0 ± 9.5	−0.027 ± 0.033	0.004 ± 0.037	7	5
0.60	−3.1 ± 10.9	202.3 ± 13.4	−0.008 ± 0.041	0.037 ± 0.043	7	5
0.88	−1.3 ± 15.9	196.8 ± 15.6	−0.041 ± 0.055	0.040 ± 0.048	7	5
1.27	6.5 ± 17.0	175.5 ± 17.9	0.014 ± 0.056	−0.027 ± 0.053	7	5
3.19	−23.5 ± 19.4	133.1 ± 25.4	−0.017 ± 0.083	−0.018 ± 0.086	7	5

Note. Column (1): radius. Column (2): LOS velocity after subtraction of systemic velocity. Column (3): LOS velocity dispersion. Column (4): third-order Gauss-Hermite coefficient. Column (5): fourth-order Gauss-Hermite coefficient. Column (6): slit position angle measured North through East. Column(7): observing run.

Table A4. Line-strength indices of the sample galaxies.

r (arcsec) (1)	H β (\AA) (2)	[MgFe] (\AA) (3)	$\langle\text{Fe}\rangle$ (\AA) (4)	Mgb (\AA) (5)	Mg ₂ (mag) (6)	PA ($^\circ$) (7)	Run (8)
NGC 7113							
-7.86	2.316 \pm 0.363	2.893 \pm 0.574	1.953 \pm 0.539	4.286 \pm 0.518	0.246 \pm 0.014	0	1
-4.19	2.290 \pm 0.215	2.989 \pm 0.343	2.242 \pm 0.332	3.983 \pm 0.325	0.263 \pm 0.009	0	1
-2.72	1.552 \pm 0.187	2.965 \pm 0.290	2.241 \pm 0.282	3.922 \pm 0.274	0.252 \pm 0.007	0	1
-1.85	1.503 \pm 0.177	3.025 \pm 0.288	2.096 \pm 0.273	4.366 \pm 0.262	0.283 \pm 0.007	0	1
-1.24	1.574 \pm 0.150	3.138 \pm 0.237	2.060 \pm 0.219	4.780 \pm 0.215	0.293 \pm 0.006	0	1
-0.64	1.444 \pm 0.123	3.083 \pm 0.184	2.263 \pm 0.178	4.198 \pm 0.173	0.278 \pm 0.005	0	1
-0.03	1.546 \pm 0.110	3.374 \pm 0.158	2.471 \pm 0.152	4.608 \pm 0.148	0.277 \pm 0.004	0	1
0.58	1.897 \pm 0.122	3.284 \pm 0.161	2.330 \pm 0.153	4.630 \pm 0.152	0.274 \pm 0.004	0	1
1.18	1.257 \pm 0.141	3.200 \pm 0.181	2.283 \pm 0.170	4.485 \pm 0.172	0.260 \pm 0.004	0	1
1.79	2.054 \pm 0.183	3.152 \pm 0.228	2.233 \pm 0.214	4.451 \pm 0.217	0.245 \pm 0.006	0	1
2.66	1.574 \pm 0.204	3.094 \pm 0.265	2.107 \pm 0.244	4.541 \pm 0.253	0.263 \pm 0.006	0	1
4.13	1.800 \pm 0.251	3.349 \pm 0.331	2.504 \pm 0.316	4.478 \pm 0.321	0.245 \pm 0.008	0	1
7.16	2.204 \pm 0.370	2.793 \pm 0.509	1.817 \pm 0.464	4.292 \pm 0.469	0.234 \pm 0.012	0	1
-7.65	1.594 \pm 0.502	0	3
-2.90	1.466 \pm 0.318	0	3
-1.74	1.548 \pm 0.298	0	3
-0.93	1.599 \pm 0.257	0	3
-0.32	1.849 \pm 0.319	0	3
0.09	2.038 \pm 0.311	0	3
0.50	1.568 \pm 0.311	0	3
1.10	1.497 \pm 0.255	0	3
1.92	2.245 \pm 0.319	0	3
3.08	2.023 \pm 0.333	0	3
7.69	2.249 \pm 0.514	0	3
-2.84	1.843 \pm 0.336	3.050 \pm 0.866	2.234 \pm 0.873	4.164 \pm 0.739	0.224 \pm 0.021	90	5
-0.91	2.238 \pm 0.136	3.206 \pm 0.406	2.562 \pm 0.430	4.012 \pm 0.343	0.283 \pm 0.010	90	5
-0.51	2.168 \pm 0.113	3.144 \pm 0.411	2.332 \pm 0.432	4.240 \pm 0.324	0.287 \pm 0.009	90	5
-0.23	1.866 \pm 0.090	3.301 \pm 0.322	2.377 \pm 0.337	4.585 \pm 0.244	0.272 \pm 0.007	90	5
0.05	1.629 \pm 0.080	3.394 \pm 0.208	2.677 \pm 0.226	4.303 \pm 0.165	0.270 \pm 0.005	90	5
0.54	1.977 \pm 0.120	3.302 \pm 0.341	2.493 \pm 0.348	4.373 \pm 0.295	0.251 \pm 0.007	90	5
2.89	2.217 \pm 0.341	3.374 \pm 0.310	2.777 \pm 0.278	4.098 \pm 0.343	0.266 \pm 0.010	90	5
PGC 1852							
-12.14	1.822 \pm 0.652	2.167 \pm 0.714	1.619 \pm 0.675	2.900 \pm 0.703	0.214 \pm 0.020	-42	1
-8.95	2.313 \pm 0.461	2.721 \pm 0.509	2.015 \pm 0.479	3.674 \pm 0.501	0.214 \pm 0.014	-42	1
-6.86	2.753 \pm 0.353	2.305 \pm 0.435	1.383 \pm 0.379	3.839 \pm 0.396	0.220 \pm 0.011	-42	1
-5.38	1.900 \pm 0.314	2.784 \pm 0.387	1.845 \pm 0.352	4.201 \pm 0.369	0.223 \pm 0.010	-42	1
-4.17	2.181 \pm 0.286	2.846 \pm 0.336	1.991 \pm 0.311	4.069 \pm 0.325	0.231 \pm 0.009	-42	1
-2.94	2.366 \pm 0.219	2.773 \pm 0.260	2.079 \pm 0.249	3.699 \pm 0.251	0.224 \pm 0.007	-42	1
-2.06	1.586 \pm 0.232	2.859 \pm 0.276	2.367 \pm 0.269	3.454 \pm 0.275	0.231 \pm 0.008	-42	1
-1.45	2.194 \pm 0.196	2.987 \pm 0.230	2.484 \pm 0.223	3.593 \pm 0.230	0.219 \pm 0.007	-42	1
-0.85	2.094 \pm 0.157	2.824 \pm 0.187	2.216 \pm 0.179	3.597 \pm 0.186	0.216 \pm 0.005	-42	1
-0.24	1.089 \pm 0.151	2.819 \pm 0.174	2.126 \pm 0.162	3.736 \pm 0.178	0.213 \pm 0.005	-42	1
0.37	1.348 \pm 0.149	2.870 \pm 0.158	2.292 \pm 0.148	3.595 \pm 0.163	0.203 \pm 0.005	-42	1
0.97	1.402 \pm 0.172	2.716 \pm 0.176	2.201 \pm 0.167	3.352 \pm 0.180	0.197 \pm 0.005	-42	1
1.58	1.665 \pm 0.203	2.755 \pm 0.200	2.109 \pm 0.189	3.600 \pm 0.202	0.211 \pm 0.006	-42	1
2.18	2.200 \pm 0.245	2.843 \pm 0.249	2.070 \pm 0.230	3.904 \pm 0.249	0.212 \pm 0.007	-42	1
3.06	1.986 \pm 0.251	2.830 \pm 0.256	2.338 \pm 0.244	3.425 \pm 0.263	0.207 \pm 0.008	-42	1
4.29	2.102 \pm 0.318	2.532 \pm 0.355	1.760 \pm 0.331	3.642 \pm 0.335	0.216 \pm 0.010	-42	1
5.51	2.160 \pm 0.353	2.734 \pm 0.387	2.414 \pm 0.382	3.096 \pm 0.387	0.209 \pm 0.011	-42	1
6.99	2.801 \pm 0.345	2.960 \pm 0.381	2.602 \pm 0.380	3.367 \pm 0.374	0.210 \pm 0.011	-42	1
9.06	1.811 \pm 0.429	2.483 \pm 0.502	2.023 \pm 0.500	3.047 \pm 0.479	0.168 \pm 0.014	-42	1
12.20	2.361 \pm 0.670	2.553 \pm 0.780	2.127 \pm 0.779	3.066 \pm 0.751	0.193 \pm 0.022	-42	1
-5.25	2.377 \pm 0.520	2.137 \pm 0.594	1.212 \pm 0.502	3.769 \pm 0.532	0.170 \pm 0.015	48	2
-1.81	2.109 \pm 0.212	2.654 \pm 0.205	2.070 \pm 0.191	3.403 \pm 0.212	0.199 \pm 0.006	48	2
-0.73	1.632 \pm 0.206	2.863 \pm 0.201	2.003 \pm 0.182	4.091 \pm 0.204	0.215 \pm 0.006	48	2
-0.12	2.300 \pm 0.172	2.945 \pm 0.173	2.194 \pm 0.160	3.955 \pm 0.175	0.199 \pm 0.005	48	2

Table A4 – continued

0.48	2.363 ± 0.167	2.779 ± 0.177	2.102 ± 0.166	3.674 ± 0.180	0.185 ± 0.005	48	2
1.34	1.791 ± 0.166	2.885 ± 0.188	2.108 ± 0.174	3.949 ± 0.188	0.175 ± 0.005	48	2
4.52	2.083 ± 0.346	2.899 ± 0.377	2.322 ± 0.367	3.619 ± 0.371	0.158 ± 0.011	48	2
NGC 67207							
-7.16	1.855 ± 0.440	2.815 ± 0.632	2.540 ± 0.658	3.119 ± 0.592	0.181 ± 0.018	-83	1
-3.87	1.437 ± 0.304	2.603 ± 0.413	2.127 ± 0.417	3.186 ± 0.386	0.202 ± 0.012	-83	1
-2.40	2.055 ± 0.232	2.552 ± 0.328	1.875 ± 0.326	3.472 ± 0.287	0.212 ± 0.009	-83	1
-1.54	1.542 ± 0.192	2.849 ± 0.285	1.969 ± 0.276	4.121 ± 0.247	0.223 ± 0.008	-83	1
-0.93	1.731 ± 0.139	3.040 ± 0.199	2.178 ± 0.197	4.243 ± 0.172	0.239 ± 0.005	-83	1
-0.33	1.682 ± 0.114	3.097 ± 0.164	2.195 ± 0.160	4.370 ± 0.143	0.249 ± 0.005	-83	1
0.28	1.723 ± 0.102	3.118 ± 0.149	2.250 ± 0.146	4.320 ± 0.132	0.246 ± 0.004	-83	1
0.88	1.774 ± 0.128	3.187 ± 0.186	2.415 ± 0.185	4.206 ± 0.168	0.227 ± 0.005	-83	1
1.49	1.582 ± 0.179	2.706 ± 0.273	1.798 ± 0.256	4.070 ± 0.242	0.213 ± 0.008	-83	1
2.35	1.327 ± 0.192	2.548 ± 0.304	1.633 ± 0.280	3.975 ± 0.269	0.200 ± 0.008	-83	1
3.82	2.088 ± 0.280	2.491 ± 0.415	1.717 ± 0.390	3.615 ± 0.382	0.192 ± 0.012	-83	1
7.11	1.678 ± 0.470	2.746 ± 0.683	2.070 ± 0.667	3.644 ± 0.639	0.198 ± 0.020	-83	1
-5.57	2.197 ± 0.608	0	3
-2.25	1.905 ± 0.333	0	3
-1.26	1.610 ± 0.324	0	3
-0.45	1.814 ± 0.324	0	3
0.37	2.149 ± 0.313	0	3
1.18	1.669 ± 0.315	0	3
1.99	2.124 ± 0.365	0	3
5.01	1.833 ± 0.468	0	3
-2.81	1.902 ± 0.504	2.716 ± 0.691	1.857 ± 0.662	3.972 ± 0.605	0.200 ± 0.032	7	5
-0.91	1.539 ± 0.275	2.746 ± 0.322	1.923 ± 0.303	3.921 ± 0.300	0.234 ± 0.016	7	5
-0.52	1.719 ± 0.124	2.858 ± 0.234	2.016 ± 0.235	4.054 ± 0.192	0.215 ± 0.010	7	5
-0.24	1.567 ± 0.116	2.982 ± 0.187	2.141 ± 0.192	4.152 ± 0.150	0.232 ± 0.007	7	5
0.04	1.821 ± 0.079	3.125 ± 0.164	2.292 ± 0.155	4.260 ± 0.158	0.247 ± 0.005	7	5
0.32	1.798 ± 0.120	3.051 ± 0.178	2.220 ± 0.181	4.194 ± 0.148	0.245 ± 0.008	7	5
0.60	1.617 ± 0.137	2.931 ± 0.228	2.121 ± 0.226	4.051 ± 0.198	0.238 ± 0.010	7	5
0.88	1.865 ± 0.226	2.777 ± 0.299	1.980 ± 0.310	3.897 ± 0.231	0.231 ± 0.014	7	5
1.27	1.565 ± 0.265	2.689 ± 0.356	1.943 ± 0.366	3.721 ± 0.283	0.222 ± 0.018	7	5
3.19	2.052 ± 0.408	2.583 ± 0.586	1.741 ± 0.564	3.830 ± 0.499	0.199 ± 0.025	7	5

Note. Column (1): radius. Columns (2)-(6): equivalent width of the line-strength indices. Column (7): slit position angle measured North through East. Column(8): observing run.